Fault-tolerant Composite Adaptive Neural Control with Safety Guarantees for Multirotors in UAM Applications

Mahdi Shahrajabian, Fariborz Saghafi*

Department of Aerospace Engineering, Sharif University of Technology, Tehran, Iran

Abstract

The demand for autonomous eVTOL aircrafts is driven by the need for innovative solutions to address transportation challenges in urban environments. Developing autonomous systems requires safety guarantees and robust control systems capable of handling uncertainties, disturbances, and faults. This paper introduces an intelligent control framework for multirotor eVTOLs in Urban Air Mobility applications. The inner-loop attitude/altitude tracking employs a Composite Adaptive Neural Control with Disturbance Observer (CANCDO); it combines Lyapunov-based neural network adaptation to compensate for uncertainties with a disturbance observer that estimates the upper bound of disturbances while compensating for estimation errors. The framework simultaneously trains the neural network and disturbance observer online by using a composite error, which includes both tracking error and state estimation error from an adaptive observer. The outer-loop horizontal position control uses a PD controller enhanced with an ESO for precise trajectory tracking. To provide fault tolerance, the framework includes a two-stage Fault Detection and Diagnosis (FDD) scheme, which estimates actuator effectiveness coefficients in real time and pairs with dynamic control allocation to optimally distribute virtual control efforts during failures. Additionally, adaptive Control Barrier Functions are developed to enforce safety constraints on position and velocity by incorporating real-time uncertainty estimates from CANCDO, which ensures safe operation even when there are model discrepancies. The framework is validated on a high-fidelity multirotor air taxi simulation model, achieving a final Relative RMSE of 0.34% for trajectory tracking under simultaneous faults and severe wind disturbances.

Keywords: Adaptive Neural Control, Fault-tolerant Control, Control Barrier Functions, Multirotor, Urban Air Mobility

1. Introduction

In recent years, advances in autonomy and intelligent control have enabled considerable improvements in safety-critical systems such as aerial vehicles, autonomous cars, and robotic platforms. These technologies have demonstrated that reliable autonomy can reduce human error, enhance operational efficiency, and extend system capabilities beyond human limitations. Extending this paradigm to passenger-carrying aerial vehicles has the potential to transform urban transportation, particularly through the deployment of electric Vertical Take-Off and Landing (eVTOL) air taxis. According to the Vertical Flight Society [1], over 800 eVTOL configurations have been explored to date, encompassing designs such as multirotor, lift-plus-cruise, and vectored-thrust aircraft.

Unlike conventional rotorcraft, multirotor eVTOL aircraft leverage Distributed Electric Propulsion (DEP) to achieve quieter, cleaner, and more cost-effective operations. Their actuator redundancy further enhances resilience, making them attractive candidates for Urban Air Mobility (UAM) networks [2]. However, these benefits can only be fully realized if eVTOLs operate with a high degree of autonomy, capable of safe and reliable performance in complex urban environments [3]. This requirement imposes stringent demands on the flight control system, which must ensure stability, precision, and safety under modeling uncertainties, environmental disturbances, and potential faults. Various control approaches have been proposed for conventional multirotors [4, 5, 6, 7, 8]. However, multirotor eVTOL air taxis, while sharing similar characteristics, are considerably less agile due to higher weight, larger moments of inertia, and slower motor responses [9]. Additionally, the aerodynamic effects on the rotors and the airframe cannot be neglected.

Neural networks (NNs) have been widely used in adaptive control over the past two decades, particularly for aerial vehicles [10, 11]. The Feedback Error Learning (FEL) approach is the most common method for integrating NNs into adaptive controllers, enabling the system to learn and compensate for unknown dynamics while satisfying Lyapunov stability [12]. FEL leverages tracking errors to update the NN and mitigate model uncertainties. To improve learning efficiency, a state observer can be employed to estimate system uncertainties, with the observer incorporates its estimation error into the NN update, a technique known as composite learning [13, 14]. Furthermore, an adaptive Disturbance Observer (DO) can compensate for residual NN estimation errors and time-varying disturbances not captured by the NN. This reduces the need for high learning rates and ensures asymptotic stability. For instance, [15] combined NNs with a DO that estimates the residual un-

*Corresponding author

Email address: saghafi@sharif.edu (Fariborz Saghafi)

certainty itself, though this design requires the additional assumption that the time derivative of the disturbance is bounded.

Guaranteeing safety in such safety-critical systems requires more than just accurate trajectory tracking [16]. A reliable system that executes commands correctly may still fail to ensure safety if those commands drive the vehicle into unsafe regions. Consequently, modern flight control systems must integrate robustness, fault tolerance, and formal safety guarantees into a unified design.

Over the past decades, significant research has been devoted to Fault-tolerant Control (FTC), specially for multirotors [17]. Passive FTC strategies employ robust control laws to tolerate predefined faults, whereas active FTC methods adapt control parameters or reconfigure commands in response to detected failures. In the field of active FTC, Fault Detection and Diagnosis (FDD) has been extensively studied, employing model-based techniques such as observers [18, 19, 20], Kalman filters [21], Recursive Least Squares (RLS) [22], parity space methods [23], as well as data-driven approaches including neural networks and machine learning classifiers [24, 25, 26].

Model-based methods rely heavily on accurate system models and can suffer from degraded performance or false alarms under model inaccuracies or unaccounted disturbances. Data-driven approaches handle nonlinearities and unmodeled dynamics but face challenges in stability guarantees, dataset requirements, and generalization to unseen faults. In [27], a sliding mode observer is proposed for robust actuator fault detection and diagnosis of an octorotor in the presence of disturbances.

In [26], an Online Sequential Extreme Learning Machine (OS-ELM) method is developed to estimate the actuator effectiveness coefficients for a quadrotor subject to actuator faults, which required the dynamics of the system. In [28], an adaptive sliding mode–based fault-tolerant control was introduced, featuring adaptive control allocation for a hexarotor. However, it considered fault estimation error while neglecting external disturbances and limiting validation to hover conditions.

In [29], a Loss of Effectiveness (LoE) estimation method is proposed for decoupling aerodynamic effects like blade flapping from faults in a quadrotor, using a reduced-order generalized Kalman filter capable of estimating multiple faults simultaneously. Khattab et al. [30] proposed a fault-tolerant control strategy for an octorotor using sliding mode control combined with weighted pseudo-inverse control allocation. However, their approach lacks a fault detection scheme and assumes that fault severity is known a priori. Despite the significant progress in FTC design, most existing studies assume constant thrust and drag moment coefficients in propeller models; they neglect the coefficients' dependence on external disturbances (e.g., wind gusts). This simplifying assumption can limit the fidelity of the system model and impair fault detection and control reconfiguration performance.

Motivated by the above discussion, this work proposes a novel adaptive neural flight control architecture for autonomous multirotor eVTOLs. The proposed approach includes an inner-loop adaptive neural controller with disturbance observers for attitude and altitude control. Additionally, it features an outer-loop PD controller augmented with an Extended State Observer (ESO) for trajectory tracking. A time-scale decomposition strategy is employed to decouple fast inner-loop dynamics from slower outer-loop dynamics, allowing independent controller design and stability analysis via Lyapunov theory. Moreover, a dynamic control allocation based on a novel two-stage FDD is proposed to cope with the simultaneous actuator faults. Beyond fault tolerance, safety requires enforcing state constraints during flight. Control Barrier Functions (CBFs) provide such guarantees but conventional designs depend on nominal models, reducing robustness under uncertainties and disturbances [31]. To address this, we propose an adaptive CBF framework that leverages uncertainty estimates from the controller, enabling real-time enforcement of safety limits and trajectory containment despite faults and environmental disturbances.

The main contributions of this thesis are:

1. A Composite-Learning-Based Adaptive Neural Control with Disturbance Observer (CANCDO) approach for multirotors is proposed to improve the quality of online uncertainty estimation and is capable of robust trajectory tracking under system uncertainties and external disturbances.
2. The closed-loop stability is carefully analyzed using the Lyapunov stability theorem. Using the introduced composite learning algorithm, both the tracking and estimation errors are asymptotically converged to zero, even considering significant internal and external disturbances. Using the proposed DO, the closed-loop system is capable of compensating for both the NN's estimation error and time-dependent external disturbances.
3. A dynamic control allocation algorithm is developed based on a novel two-stage robust FDD framework, combining aEKF and OS-ELM approaches to handle simultaneous actuator faults.
4. Adaptive CBFs as safety filters are proposed for enforcing safety constraints on critical states and guaranteeing operation within safe flight envelopes.
5. A high-fidelity simulation framework incorporating gyroscopic effects, rotor and body aerodynamic effects, ground effect, and wind disturbances is developed to evaluate the proposed methods under realistic urban flight scenarios.

2. Problem Formulation

2.1. Equations of Motion

The schematic of the vehicle with the Earth and Body reference frames is shown in Figure 1. The Earth frame is treated as the inertial frame, where the Earth is assumed to be flat and non-rotating. A local North–East–Down (NED) coordinate system, denoted by $]^L$, is defined based on the Earth frame and fixed to the Earth. The multirotor air taxi is then modeled as a rigid multi-body system. To demonstrate the effectiveness of the proposed control framework in UAM, the Volocopter 2X multirotor configuration is considered. To the best of our knowledge, the detailed modeling and intelligent control of this novel air-taxi configuration have not yet been investigated in the literature. The compact final form of the 6-DOF nonlinear dynamic

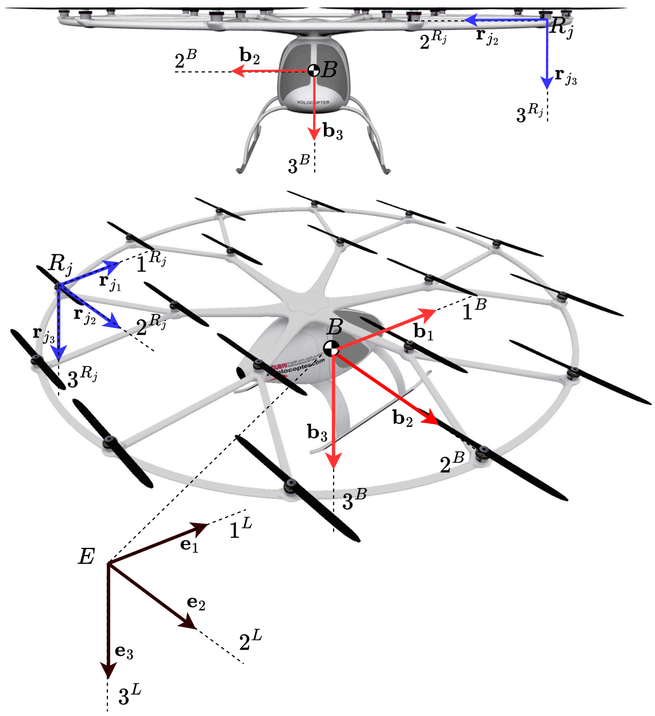

Figure 1: Schematic of the vehicle with Earth and Body frames

model of the multirotor air taxi, developed in this work using the notation of [32], is given by:

$$\left[\frac{\mathrm{d}\mathbf{v}_B^E}{\mathrm{d}t}\right]^B = \frac{1}{m}\left[\mathbf{f}_a\right]^B + \frac{1}{m}\left[\mathbf{f}_p\right]^B - \left[\mathbf{\Omega}^{BE}\right]^B\left[\mathbf{v}_B^E\right]^B + \left[\mathbf{T}\right]^{BL}\left[\mathbf{g}\right]^L, \tag{1a}$$

$$\left[\frac{\mathrm{d}\mathbf{s}_{BE}}{dt}\right]^L = \left[\bar{\mathbf{T}}\right]^{BL}\left[\mathbf{v}_B^E\right]^B, \tag{1b}$$

$$\begin{aligned}\left[\frac{\mathrm{d}\boldsymbol{\omega}^{BE}}{dt}\right]^B = {} & \left(\left[\mathbf{I}_B^B\right]^B\right)^{-1}\Big(\left[\mathbf{m}_B\right]^B - \left[\mathbf{m}_{I_R}\right]^B - \left[\mathbf{m}_{G_R}\right]^B \\ & - \left[\mathbf{\Omega}^{BE}\right]^B\left[\mathbf{I}_B^B\right]^B\left[\boldsymbol{\omega}^{BE}\right]^B\Big),\end{aligned} \tag{1c}$$

$$\dot{\mathbf{\Phi}} = \mathbf{T}_{\mathbf{\Phi}}\left[\boldsymbol{\omega}^{BE}\right]^B, \tag{1d}$$

where $\left[\overline{\mathbf{v}_B^E}\right]^B = \begin{bmatrix} u & v & w\end{bmatrix}$, $\left[\overline{\boldsymbol{\omega}^{BE}}\right]^B = \begin{bmatrix} p & q & r\end{bmatrix}$, $\left[\overline{\mathbf{s}_{BE}}\right]^L = \begin{bmatrix} x & y & z\end{bmatrix}$, $\overline{\mathbf{\Phi}} = \begin{bmatrix}\phi & \theta & \psi\end{bmatrix}$, m, and $\left[\mathbf{I}_B^B\right]^B$ represent the vehicle's velocity and angular velocity in the body coordinate system, the position of the vehicle with respect to the inertial frame, the attitude of the vehicle represented by Euler angles, the total vehicle mass, and the moment of inertia matrix, respectively.

Also $[\mathbf{f}_a]^B$, $\left[\mathbf{f}_p\right]^B$, $[\mathbf{g}]^L$, $[\mathbf{m}_B]^B$, $[\mathbf{m}_{I_R}]^B$, and $[\mathbf{m}_{G_R}]^B$ denote the total aerodynamic and propulsion forces acting on the vehicle, the gravity acceleration vector, the external moments acting on the vehicle, the inertial reaction moments, and the gyroscopic moments acting on the vehicle represented in the body coordinate system. Moreover, transformation matrices $[\mathbf{T}]^{BL}$ and $\mathbf{T}_{\mathbf{\Phi}}$ are defined as follows:

$$[\mathbf{T}]^{BL} = \begin{bmatrix} \mathrm{C}\theta\mathrm{C}\psi & \mathrm{C}\theta\mathrm{S}\psi & -\mathrm{S}\theta \\ \mathrm{S}\phi\mathrm{S}\theta\mathrm{C}\psi - \mathrm{C}\phi\mathrm{S}\psi & \mathrm{S}\phi\mathrm{S}\theta\mathrm{S}\psi + \mathrm{C}\phi\mathrm{C}\psi & \mathrm{S}\phi\mathrm{C}\theta \\ \mathrm{C}\phi\mathrm{S}\theta\mathrm{C}\psi + \mathrm{S}\phi\mathrm{S}\psi & \mathrm{C}\phi\mathrm{S}\theta\mathrm{S}\psi - \mathrm{S}\phi\mathrm{C}\psi & \mathrm{C}\phi\mathrm{C}\theta \end{bmatrix}, \tag{2}$$

$$\mathbf{T}_{\Phi} = \begin{bmatrix} 1 & \sin\phi\tan\theta & \cos\phi\tan\theta \\ 0 & \cos\phi & -\sin\phi \\ 0 & \sin\phi\sec\theta & \cos\phi\sec\theta \end{bmatrix}, \tag{3}$$

where S and C represent the sine and cosine functions, respectively. It should be noted that $\bar{\mathbf{a}}$ represents the matrix transpose of $\mathbf{a}$ and the skew-symmetric matrix of angular velocity $\left[\mathbf{\Omega}^{BE}\right]^B$ is defined as follows:

$$\left[\mathbf{\Omega}^{BE}\right]^B = \begin{bmatrix} 0 & -r & q \\ r & 0 & -p \\ -q & p & 0 \end{bmatrix}. \tag{4}$$

2.2. Forces and Moments Model

Given that, in general, aerodynamic forces and moments are a function of relative velocity (velocity of the vehicle relative to the air), it is important to model and apply the effect of wind and turbulence as external disturbances. By defining an air frame with the symbol @, the relative velocity of the CoG with respect to the atmosphere in the body coordinate system $\left[\overline{\mathbf{v}_B^@}\right]^B = [\, u_{rv} \quad v_{rv} \quad w_{rv}\,]$ can be expressed as follows:

$$\left[\mathbf{v}_B^@\right]^B = \left[\mathbf{v}_B^E\right]^B - [\mathbf{T}]^{BL}\left[\mathbf{v}_@^E\right]^L, \tag{5}$$

where $\left[\mathbf{v}_@^E\right]^L$ represents the total air velocity (wind and turbulence) relative to the ground in the local earth coordinate system. Also, V_{rv} represents the magnitude of the relative velocity $\left[\mathbf{v}_B^@\right]^B$. In general, wind can include steady wind, wind shear, gust, and atmospheric turbulence. Of these, atmospheric turbulence is stochastic in nature, and the rest is deterministic. For details on the modeling of winds, see Appendix A.

Figure 2 shows the rotational directions of the rotors. Based on the given geometry, the position of the jth rotor center is expressed as:

$$\left[\overline{\mathbf{s}_{R_jB}}\right]^B = \begin{bmatrix}\ell_j\cos\beta_j & \ell_j\sin\beta_j & -h_r\end{bmatrix}, \tag{6}$$

where h_r is the vertical distance between the actuator's plane and the CoG of the vehicle. According to (4) and (6), the translational velocity of the jth rotor with respect to the atmosphere in the body coordinate can be written as follows:

$$\left[\mathbf{v}_{R_j}^@\right]^B = \begin{bmatrix} u_{R_j} \\ v_{R_j} \\ w_{R_j}\end{bmatrix} = \left[\mathbf{v}_B^@\right]^B + \left[\mathbf{\Omega}^{BE}\right]^B\left[\mathbf{s}_{R_jB}\right]^B \tag{7}$$

Also, the total propulsion force vector can be modeled as follows:

$$\left[\overline{\mathbf{f}_p}\right]^B = \begin{bmatrix}0 & 0 & -F_T\end{bmatrix}, \tag{8}$$

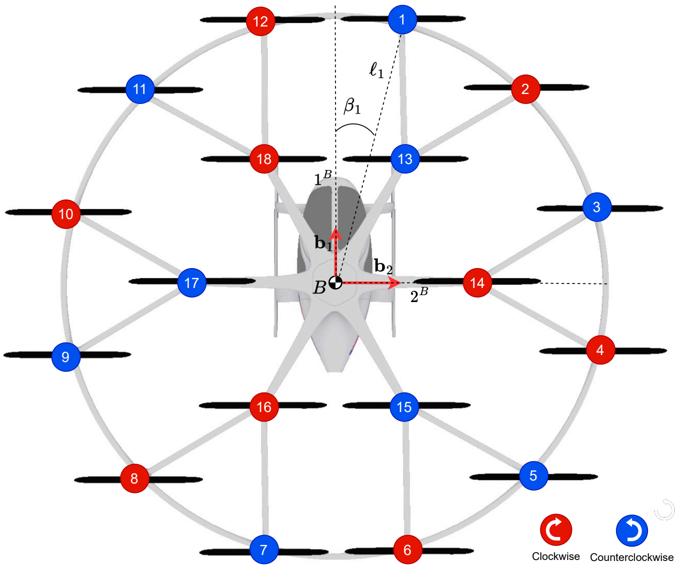

Figure 2: Rotation configuration of the motors

where F_T is the summation of all generated thrust forces f_j by the rotors. Additionally, the aerodynamic forces acting on the vehicle are modeled as follows:

$$\begin{aligned}[\mathbf{f}_a]^B &= [\mathbf{f}_{D,b}]^B + [\mathbf{f}_{D,R}]^B \\ &= -\frac{1}{2}\rho \begin{bmatrix} C_{D_x} S_x u_{rv}|u_{rv}| \\ C_{D_y} S_y v_{rv}|v_{rv}| \\ C_{D_z} S_z w_{rv}|w_{rv}| \end{bmatrix} \\ &+ \sum_{j=1}^{N_R} \begin{bmatrix} H_{x,j} \\ H_{y,j} \\ 3\left(\frac{1}{2}\rho C_{D_{\text{rod}}} S_{\text{rod}} \left(-w_{R_j} + v_{i,j}\right)^2\right) \end{bmatrix},\end{aligned} \tag{9}$$

where C_{D_x}, C_{D_y} and C_{D_z} represent the drag coefficients in three directions and S_x, S_y and S_z represent the base area in three directions. In addition, $C_{D_{\text{rod}}}$ and S_{rod} represent the drag coefficient of of each individual rod forming the three-branch structure located beneath a rotor and the reference area of the rod, respectively.

The torques acting on the vehicle can be considered to be due to the rotor torque $\mathbf{m}_R$ and external torques $\mathbf{m}_d$:

$$\begin{aligned}[\mathbf{m}_B]^B &= [\mathbf{m}_R]^B + [\mathbf{m}_d]^B \\ &= \sum_{j=1}^{N_R} \left(\left[\overline{\mathbf{m}_{R_j}}\right]^B + \left[\mathbf{S}_{R_j B}\right]^B \left[\overline{\mathbf{f}_{R_j}}\right]^B\right) + [\mathbf{m}_d]^B\end{aligned} \tag{10}$$

The torque generated by the rotors consists of two parts: the torque generated by the resistance to the rotation of the rotor and the torque generated by the forces generated by the rotor based on the arm of each rotor relative to the CoG. Considering the constant angle of installation of the motors, the torque generated by each rotor due to drag can be expressed in the body coordinate system as follows:

$$\left[\overline{\mathbf{m}_{R_j}}\right]^B = \begin{bmatrix} 0 & 0 & -\epsilon_j \tau_j \end{bmatrix}, \tag{11}$$

where, according to the configuration of the vehicle given in Figure 2, $\epsilon_j = (-1)^j$. Furthermore, the force produced by each rotor in the body coordinate system can be expressed as:

$$\left[\overline{\mathbf{f}_{R_j}}\right]^B = \begin{bmatrix} H_{x,j} & H_{y,j} & -f_j \end{bmatrix}, \tag{12}$$

where H represents the horizontal force on the rotor plane. Therefore, the total generated moments by the rotors is as follows:

$$\begin{aligned}[\mathbf{m}_R]^B &= [\mathbf{m}_C]^B + [\mathbf{m}_H]^B \\ &= \sum_{j=1}^{N_R} \begin{bmatrix} -f_j \ell_j \sin\beta_j \\ f_j \ell_j \cos\beta_j \\ -\epsilon_j \tau_j \end{bmatrix} + \sum_{j=1}^{N_R} \begin{bmatrix} h_r H_{y,j} \\ -h_r H_{x,j} \\ -H_{x,j}\ell_j \sin\beta_j + H_{y,j}\ell_j \cos\beta_j \end{bmatrix},\end{aligned} \tag{13}$$

where $[\overline{\mathbf{m}_C}]^B = \begin{bmatrix} \tau_x & \tau_y & \tau_z \end{bmatrix}$ represents control moments. Moreover, the inertial reaction and gyroscopic moments are obtained as

$$[\overline{\mathbf{m}_{I_R}}]^B = \sum_{j=1}^{N_R} \begin{bmatrix} 0 & 0 & I_R \epsilon_j \dot{\omega}_{R_j} \end{bmatrix} \tag{14}$$

$$[\mathbf{m}_{G_R}]^B = \left[\mathbf{\Omega}^{BE}\right]^B \sum_{j=1}^{N_R} \begin{bmatrix} 0 \\ 0 \\ I_R \epsilon_j \omega_{R_j} \end{bmatrix}, \tag{15}$$

where ω_{R_j} is the speed of the jth rotor. Furthermore, $\epsilon_j = \pm 1$ indicates the direction of rotation of the rotor, which is $+1$ if it is clockwise and -1 if it is counterclockwise. Also, I_R denotes the rotor (total motor and propeller) axial moment of inertia.

The magnitude of the forces and moments of a rotor is modeled as follows:

$$f = \frac{1}{2}\rho\pi R_p^4 C_f \omega_R^2 = b\omega_R^2 \tag{16a}$$

$$H = \frac{1}{2}\rho\pi R_p^4 C_H \omega_R^2 = h_f \omega_R^2 \tag{16b}$$

$$\tau = \frac{1}{2}\rho\pi R_p^5 C_\tau \omega_R^2 = d\omega_R^2, \tag{16c}$$

where ρ, R_p and ω_R represent the air density, propeller radius, and rotor speed, respectively. Inspired by [33] we can obtain the forces and moment coefficients in (16) based on the Blade Element Momentum Theory (BEMT) as follows:

$$C_f = 0.0386 + 0.0705\,\mu^2 - 0.182\,\lambda \tag{17a}$$

$$C_\tau = 0.00077 + 0.00118\,\mu^2 - 0.148\,\lambda^2 + 0.031\,\lambda \tag{17b}$$

$$C_H = 0.00236\,\mu + 0.0546\,\lambda\,\mu, \tag{17c}$$

where

$$\lambda_c = \frac{w_R}{\omega_R R_p}, \tag{18a}$$

$$\lambda_i = \frac{v_i}{\omega_R R_p}, \tag{18b}$$

$$\lambda = \lambda_c + \lambda_i, \tag{18c}$$

$$\mu = \frac{V_h}{\omega_R R_p}. \tag{18d}$$

In the aforementioned definitions, v_i, λ_i, λ_c and μ indicate induced velocity, induced inflow ratio, climb ratio, and advance ratio, respectively. Additionally, $V_h = \sqrt{u_R^2 + v_R^2}$ is the magnitude of the horizontal velocity in the rotor's plane. It is worth noting that, unlike the linear relation in [33], we fitted a 4th-order polynomial to the propeller's chord c_b curve using T-MOTOR NS47*18 propeller geometry data [34]. Moreover, the unknown coefficients of the propeller lift, drag, and pitch (twist) angle are determined based on the experimental data obtained from the static condition tests [34].

In order to find the induced inflow ratio or equivalently induced velocity that appears in (17), (19) must be numerically solved in each simulation time step. In this work, the Newton-Raphson method is utilized due to its high convergence speed.

$$c_1 + c_2(\lambda_i + \lambda_c) + c_3\mu^2 - 4\lambda_i\sqrt{(\lambda_i + \lambda_c)^2 + \mu^2} = 0. \tag{19}$$

where c_1, c_2 and c_3 are known constants that can be determined from experimental test data in static condition. Therefore, unlike existing works that consider constant coefficients for rotor's thrust and torque, in this paper the coefficients b and d vary based on the environmental conditions and the rotor's horizontal force effects are taken into account.

In this work, the Hayden model is utilized to include the ground effect on the generated thrust forces near surfaces such as ground or building roofs [35, 36]:

$$f_{IGE} = \left(0.9926 + 0.03794\left(\frac{2R_p}{h_b + h_r}\right)^2\right) f = K_G(h_r)f, \tag{20}$$

where h_b is the overall height of the air taxi body, h_r is the relative height of the vehicle to the surface, and R_p is the propeller radius. Thus, the ground effect is applied to the obtained thrust force from BEMT with a correction factor as a function of the relative height.

2.3. Actuator Model

The multirotor air taxi actuator system consists of the battery, Brushless Direct Current (BLDC) motor, propeller, and Electronic Speed Controller (ESC).

The battery is responsible for providing the required power, and the ESC is responsible for generating the appropriate voltage to drive the motor speed to the desired speed based on the value of the Pulse Width Modulation (PWM) signal. The motor converts electrical power into mechanical power, which is accompanied by power loss due to friction and damping effects. The power given to the propeller is then converted into thrust and drag torque.

The voltage applied to each motor is modeled as

$$V_{m,j} = \sigma_j V_b, \quad j = 1, \ldots, N_R, \tag{21}$$

where σ_j is the throttle command value for each motor (the PWM value mapped to the range [0 1]), and V_b is the battery voltage. Moreover, the dynamics of the BLDC motor is considered as follows [37]:

$$L\frac{\mathrm{d}I_m}{\mathrm{d}t} = V_m - R_a I_m - K_e\omega_R \tag{22a}$$

$$I_R\frac{\mathrm{d}\omega_R}{\mathrm{d}t} = K_t I_m - B_m\omega_R - \tau, \tag{22b}$$

where I_m, L, V_m, R_a, K_e, K_t, B_m and τ respectively represent the current of the motor armature, the armature inductance, the input voltage applied to the armature, the equivalent resistance, the back-EMF constant, the motor torque constant, the damping coefficient (mechanical friction or viscous losses), and the aerodynamic torque due to the drag effects of the rotor rotation.

For advanced BLDC motors, the motor inductance is very small, effectively resulting in a very small time constant in the current dynamics [3]. In other words, it can be assumed that the electric current response is instantaneous with an approximation of $L \approx 0$. Thus, the equations can be rewritten as:

$$\begin{aligned} I_m &= \mathrm{Sat}\left(\frac{1}{R_a}\left(V_m - K_e\omega_R\right), 0, I_{\max}\right), \\ I_R\frac{\mathrm{d}\omega_R}{\mathrm{d}t} &= K_e I_m - B_m\omega_R - d\omega_R^2 \end{aligned} \tag{23}$$

where Sat represents the saturation function, which limits the current between zero and the maximum current.

3. Control System Design

As can be seen in Figure 3, the control system is cascaded and has two inner and outer loops. The outer loop is responsible for generating the desired roll and pitch angles, which, as a result of adjusting these angles, allow the air taxi to reach the acceleration required to track the reference path. The inner loop is responsible for controlling the air taxi's attitude and altitude in the presence of uncertainties and disturbances, and compensates for fault detection errors. Also, the motor fault coefficients are estimated by the fault detection and identification module and are used online in the control allocation to provide fault tolerance.

3.1. Inner-Loop Control

To design the inner-loop adaptive neural control system, the nonlinear state-space representation of the inner-loop dynamic model must be determined. Thus, by approximating $\dot{\phi} \approx p, \dot{\theta} \approx q, \dot{\psi} \approx r$, we can consider the inner-loop dynamic model (1c) as (24) with a nominal model, an uncertainty term $\mathbf{\Delta}$, and a time-varying disturbance term:

$$\ddot{\mathbf{x}} = \mathbf{F}(\dot{\mathbf{x}}) + \mathbf{B}(\mathbf{x})\boldsymbol{\nu} + \mathbf{\Delta}(\mathcal{X}, \boldsymbol{\nu}) + \mathbf{d}(t), \tag{24}$$

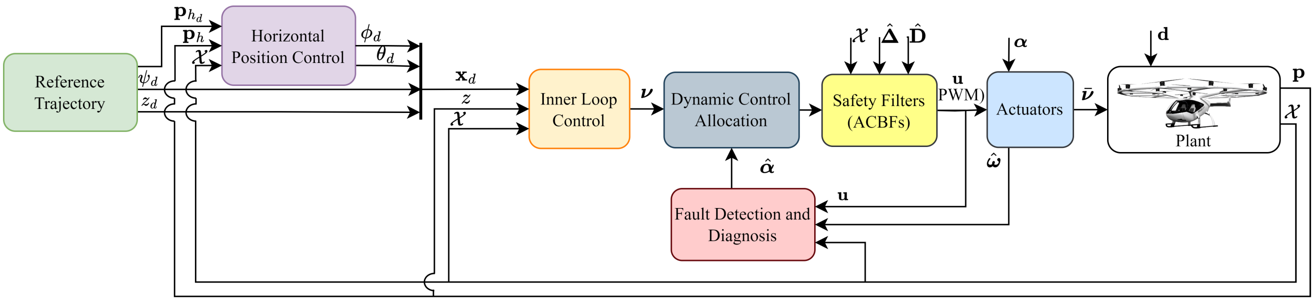

Figure 3: Overall view of the proposed control system

where

$$\mathbf{F}(\dot{\mathbf{x}}) = \begin{bmatrix} \frac{1}{I_{xx}I_{zz} - I_{xz}^2}\left((I_{yy}I_{zz} - I_{zz}^2 - I_{xz}^2)\dot{\theta}\dot{\psi} + I_{xz}(I_{yy} - I_{xx} - I_{zz})\dot{\phi}\dot{\theta}\right) \\ \frac{1}{I_{yy}}\left((I_{zz} - I_{xx})\dot{\phi}\dot{\psi} + I_{xz}(\dot{\phi}^2 - \dot{\psi}^2)\right) \\ \frac{1}{I_{xx}I_{zz} - I_{xz}^2}\left((I_{xx}^2 - I_{xx}I_{yy} + I_{xz}^2)\dot{\phi}\dot{\theta} + I_{xz}(I_{zz} + I_{xx} - I_{yy})\dot{\theta}\dot{\psi}\right) \\ g \end{bmatrix} \tag{25a}$$

$$\mathbf{B}(\mathbf{x}) = \begin{bmatrix} 0 & \frac{I_{zz}}{I_{xx}I_{zz} - I_{xz}^2} & 0 & -\frac{I_{xz}}{I_{xx}I_{zz} - I_{xz}^2} \\ 0 & 0 & \frac{1}{I_{yy}} & 0 \\ 0 & -\frac{I_{xz}}{I_{xx}I_{zz} - I_{xz}^2} & 0 & \frac{I_{xx}}{I_{xx}I_{zz} - I_{xz}^2} \\ -\frac{1}{m}\cos\theta\cos\phi & 0 & 0 & 0 \end{bmatrix}, \tag{25b}$$

where $\mathbf{x} = \begin{bmatrix}\phi & \theta & \psi & z\end{bmatrix}^\top$ and $\boldsymbol{\nu} = \begin{bmatrix}F_T & \tau_x & \tau_y & \tau_z\end{bmatrix}^\top$ represent the inner-loop variables and the virtual control input, respectively. Also, we have $\mathcal{X} = \begin{bmatrix}\boldsymbol{\Phi}^\top & \omega_{be}^\top & \mathbf{v}^\top\end{bmatrix}^\top$ where $\boldsymbol{\Phi} = \begin{bmatrix}\phi & \theta & \psi\end{bmatrix}^\top$, $\omega_{be} = \begin{bmatrix}\omega^{BE}\end{bmatrix}^B$, and $\mathbf{v} = \begin{bmatrix}\mathbf{v}_B^E\end{bmatrix}^B$. Thus, the effect of the approximation of small Euler angles, gyroscopic effects, rotor reactions, aerodynamic forces and moments, and other uncertainties are taken into account in $\boldsymbol{\Delta}$ and $\mathbf{d}(t)$, hence the nominal model has a simpler structure.

Assumption 3.1. It is assumed that uncertainties and external disturbances are bounded, i.e., $\|\boldsymbol{\Delta}\| \leq \bar{\Delta}$ and $\|\mathbf{d}\| \leq \bar{d}$, where $\bar{\Delta}$ and $\bar{d}$ are positive constants.

We estimate the uncertainty term $\boldsymbol{\Delta} \in \mathbb{R}^m$ by a neural network as follows

$$\boldsymbol{\Delta}(\mathcal{X}, \boldsymbol{\nu}) = \mathbf{W}^{*^\top}\boldsymbol{\mu}(\mathcal{X}, \boldsymbol{\nu}) + \boldsymbol{\varepsilon} \tag{26a}$$

$$\hat{\boldsymbol{\Delta}}(\mathcal{X}, \boldsymbol{\nu}) = \hat{\mathbf{W}}^\top\boldsymbol{\mu}(\mathcal{X}, \boldsymbol{\nu}), \tag{26b}$$

where $\mathbf{W}^* \in \mathbb{R}^{N_n \times m}$, $\hat{\mathbf{W}} \in \mathbb{R}^{N_n \times m}$, $\boldsymbol{\mu}(\boldsymbol{\xi}) : \mathbb{R}^n \to \mathbb{R}^{N_n}$ and $\boldsymbol{\varepsilon} \in \mathbb{R}^m$ represent the optimal (unknown) weights, the estimated weights, the vector of basis functions, and the network estimation error, respectively. The basis functions of the neural network in this study are considered as radial basis functions (RBFs):

$$\mu_i(\boldsymbol{\xi}) = \exp\left\{-\frac{(\boldsymbol{\xi} - \mathbf{c}_i)^\top(\boldsymbol{\xi} - \mathbf{c}_i)}{2\sigma_i^2}\right\}; \quad i = 1, 2, \ldots, N_n, \tag{27}$$

where $\boldsymbol{\xi} = \begin{bmatrix}\mathcal{X}^\top & \boldsymbol{\nu}^\top\end{bmatrix} \in \mathbb{R}^n$, $\mathbf{c}_i \in \mathbb{R}^n$ and σ_i represent the neural network input, the center vector, and the width of the ith basis function, respectively, and N_n specifies the number of neurons of the network. It should be noted that for better training of the neural network, the network input is usually normalized, which in this study the Z-Score approach is used, whose output data has a mean of zero and a standard deviation of one.

As a practical method to reduce the computational burden for online training of adaptive neural networks, the Extreme Learning Machine (ELM) approach is used, in which the center and weight of each neuron are randomly selected at the beginning of simulation and training and remain constant. In this approach, the neural network is usually considered with one hidden layer, but if more layers are considered, only the weights of the last layer are updated. It has also been shown that the RBF neural network with the ELM approach has the property of universal approximation [38]. Thus, to estimate the nonlinear function $\mathbf{f}(\boldsymbol{\xi})$, we have:

$$\left\|\mathbf{f}(\boldsymbol{\xi}) - \mathbf{W}^\top\boldsymbol{\mu}(\boldsymbol{\xi})\right\| \leq \varepsilon_M, \tag{28}$$

where ε_M is the upper bound of estimation error, indicating the bounded estimation error.

We define the total disturbance as $\mathbf{D}(t) = \mathbf{d}(t) + \boldsymbol{\varepsilon}$ and assume that this disturbance is bounded:

$$|\mathbf{D}| \preceq \mathbf{D}_M, \tag{29}$$

where $\preceq$ denotes an element-wise inequality.

In the case of a tracking control problem, the control objective is to design a control system such that the tracking error $\mathbf{e} = \mathbf{x} - \mathbf{x}_d$ converges to zero (or a compact neighborhood of zero). Since the system is second-order, the filtered error signal (sliding surface) is defined as follows:

$$\mathbf{s} = \dot{\mathbf{e}} + \lambda\mathbf{e} \tag{30}$$

In the Composite (Error) Learning approach, a state observer is used, and the state estimation error is utilized in the neural network weight update rule and the disturbance observer. In other words, a composite error is defined based on the tracking error and the state estimation error. Considering the state estimation error as $\mathbf{e}_s = \hat{\mathbf{x}} - \mathbf{x}$, the filtered estimation error is defined as follows:

$$\mathbf{s}_s = \dot{\mathbf{e}}_s + \lambda_s \mathbf{e}_s \tag{31}$$

Furthermore, the state observer is defined follows:

$$\ddot{\hat{\mathbf{x}}} = \mathbf{F}(\mathbf{x}, \dot{\mathbf{x}}) + \mathbf{B}(\mathbf{x})\boldsymbol{\nu}_c + \hat{\boldsymbol{\Delta}}(\mathcal{X}, \boldsymbol{\nu}) + \hat{\mathbf{D}}(t) - k_c \mathbf{s}_s - \lambda_s \dot{\mathbf{e}}_s \tag{32}$$

To account for the constraints on the (virtual) control inputs, the Modified Tracking Error (MTE) approach is adopted. Thus, we define the auxiliary variable $\boldsymbol{\gamma}$ as follows:

$$\dot{\boldsymbol{\gamma}} = -\mathbf{K}\boldsymbol{\gamma} + \mathbf{B}(\mathbf{x})(\boldsymbol{\nu} - \boldsymbol{\nu}_c) \tag{33}$$

where $\mathbf{K}$ is a definite positive diagonal matrix and is also used in the control law that determines the speed of reaching the sliding surface. Also, $\boldsymbol{\nu}$ and $\boldsymbol{\nu}_c$ represent the virtual control input with the constraint applied by the saturation function and the desired virtual input produced by the controller, respectively. Thus, the filtered MTE is defined as follows:

$$\mathbf{s}_m = \mathbf{s} - \boldsymbol{\gamma} \tag{34}$$

Note that in the absence of input constraints, $\boldsymbol{\gamma}$ approaches zero, so that the MTE coincides with the true error [12]. In addition, the disturbance observer is designed as follows:

$$\hat{\mathbf{D}} = \hat{\mathbf{D}}_M \odot \operatorname{sign}(\mathbf{e}_c), \tag{35}$$

where $\odot$ and $\hat{\mathbf{D}}_M$ represent the element-wise product and the upper bound vector estimate of the disturbance, respectively. As a result, the disturbance observer estimates the time-varying uncertainties and the neural network estimation error, and by using this estimate in the control law, its effect on the system performance can be compensated.

According to the above definitions, we design the control law as follows:

$$\boldsymbol{\nu}_c = \mathbf{B}^{-1}\left(\ddot{\mathbf{x}}_d - \mathbf{F} - \hat{\mathbf{W}}^\top \boldsymbol{\mu} - \hat{\mathbf{D}}_M \odot \operatorname{sign}(\mathbf{e}_c) - \lambda \dot{\mathbf{e}} - \mathbf{K}\mathbf{s}\right) \tag{36}$$

We design the update rules of the neural network and disturbance observer as follows:

$$\dot{\hat{\mathbf{W}}} = \Gamma \boldsymbol{\mu} \mathbf{e}_c^\top \tag{37a}$$

$$\dot{\hat{\mathbf{D}}}_M = k_D |\mathbf{e}_c| \tag{37b}$$

where Γ and k_D denote the learning rate of the neural network and the update rate of the disturbance observer, respectively.

Theorem 3.1. Using the control law (36) and the updating rules (37a)-(37b), the inner-loop would be asymptotically stable.

Proof. see Appendix B. □

Remark 3.1. The inclusion of the sign function in the control law (36) and the disturbance observer (35) introduces the well-known issue of chattering in the control signal. To address this, various techniques have been proposed in the literature. A common approach—also adopted in this work—is to replace the sign function with the smooth tanh function. In this case, the following inequality from [39] holds:

$$0 \leq |e| - e \tanh\left(\frac{e}{\epsilon_e}\right) \leq 0.2785\epsilon_e, \quad \epsilon_e > 0. \tag{38}$$

Accordingly, instead of using $|\mathbf{e}_c|$ in (37b), which is equivalent to $\mathbf{e}_c \odot \operatorname{sign}(\mathbf{e}_c)$, we employ the smoother form $\mathbf{e}_c \odot \tanh(\mathbf{e}_c/\epsilon_e)$. By adopting this modification, the closed-loop system no longer guarantees asymptotic stability; rather, we establish Uniformly Ultimately Bounded (UUB) stability, ensuring that the tracking error remains bounded [12].

Remark 3.2. The updating rules (37a)–(37b) may suffer from parameter drift in the absence of persistent excitation. To prevent this, the e-modification technique [40] is applied, which ensures bounded neural network parameters [41]. Therefore, the modified update rules are expressed as:

$$\dot{\hat{\mathbf{W}}} = \Gamma\left(\boldsymbol{\mu}\mathbf{e}_c^\top - \sigma_W |\mathbf{e}_c^\top| \odot \hat{\mathbf{W}}\right), \tag{39a}$$

$$\dot{\hat{\mathbf{D}}}_M = k_D\left(\mathbf{e}_c \odot \tanh(\mathbf{e}_c/\epsilon_e) - \sigma_{D_M}|\mathbf{e}_c| \odot \hat{\mathbf{D}}_M\right), \tag{39b}$$

where $|\mathbf{e}_c^\top| \odot \hat{\mathbf{W}}$ indicates element-wise multiplication of each column of the weight matrix $\hat{\mathbf{W}}$ by the vector $|\mathbf{e}_c^\top|$. Here, $\sigma_W > 0$ and $\sigma_{D_M} > 0$ denote design parameters. It has been proven that this modification guarantees boundedness of the neural network parameters. However, the e-modification changes the closed-loop property from asymptotic stability to UUB stability, ensuring that the tracking error remains bounded [41, 12].

The overall view of the proposed inner-loop control system is shown in Figure 4.

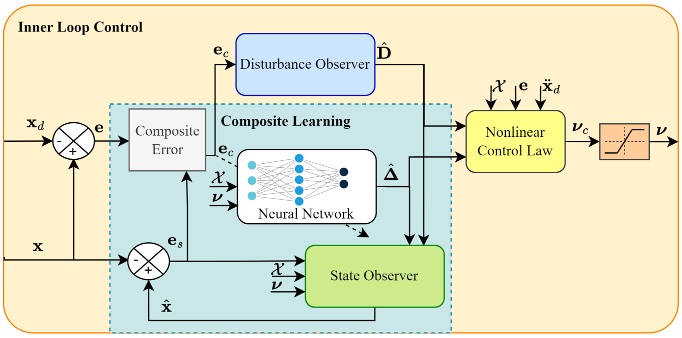

Figure 4: Overall view of the proposed inner-loop control system

3.2. Dynamic Control Allocation

Control allocation is defined as the problem of distributing virtual control (total thrust command and control torques) among the actuators [17]. The control input is defined as the vector of thrust forces:

$$\mathbf{u} = \begin{bmatrix} f_1 & f_2 & \cdots f_{N_R} \end{bmatrix}^\top. \tag{40}$$

The linear transformation between the control input and the virtual control input is expressed as follows:

$$\boldsymbol{\nu} = \mathbf{G}\mathbf{u}, \tag{41}$$

where $\mathbf{G} \in \mathbb{R}^{4\times N_R}$ is the control allocation (control effectiveness) matrix. A more precise representation of the linear transformation of the control inputs in (41) is as follows:

$$\begin{bmatrix} F_T \\ \tau_x \\ \tau_y \\ \tau_z \end{bmatrix} = \underbrace{\begin{bmatrix} 1 & 1 & \cdots & 1 \\ -\ell_1 \sin\beta_1 & -\ell_2 \sin\beta_2 & \cdots & -\ell_{N_R} \sin\beta_{N_R} \\ \ell_1 \cos\beta_1 & \ell_2 \cos\beta_2 & \cdots & \ell_{N_R} \cos\beta_{N_R} \\ -\epsilon_1 \dfrac{d_s}{b_s} & -\epsilon_2 \dfrac{d_s}{b_s} & \cdots & -\epsilon_{N_R} \dfrac{d_s}{b_s} \end{bmatrix}}_{\mathbf{G}} \begin{bmatrix} f_1 \\ f_2 \\ \vdots \\ f_{N_R}. \end{bmatrix} \tag{42}$$

A diagonal matrix $\mathbf{L}$, denoting the actuator health weighting, is defined as follows:

$$\mathbf{L} = \mathrm{diag}\left(\begin{bmatrix}\alpha_1 & \alpha_2 & \cdots & \alpha_{N_R}\end{bmatrix}\right), \tag{43}$$

where $0 \leq \alpha_j \leq 1$ represents the level of health of the actuator, such that $\alpha_j = 0$ indicates complete failure of the actuator and $\alpha_j = 1$ indicates flawless operation. Also, in the condition $0 < \alpha_j < 1$, the jth actuator has a loss of effectiveness (LoE).

The linear transformation relationship between the control input and the virtual control in the general condition of fault occurrence is rewritten as follows:

$$\boldsymbol{\nu} = \mathbf{GLu} \tag{44}$$

Therefore, the optimization problem of control allocation is defined as follows:

$$\begin{aligned} \min_{\mathbf{u}} \quad & \|\mathbf{u}\|^2 \\ \text{s.t.} \quad & \boldsymbol{\nu} = \mathbf{GLu} \end{aligned} \tag{45}$$

Using the Lagrange multipliers method to solve the aforementioned optimization problem, the optimal control inputs is obtained as follows:

$$\mathbf{u} = (\mathbf{G}\hat{\mathbf{L}})^\top \left((\mathbf{G}\hat{\mathbf{L}})(\mathbf{G}\hat{\mathbf{L}})^\top\right)^{-1} \boldsymbol{\nu} = \bar{\mathbf{G}}^\dagger \boldsymbol{\nu} \tag{46}$$

where $\bar{\mathbf{G}} = \mathbf{G}\hat{\mathbf{L}}$ and $\hat{\mathbf{L}}$ is the estimation of $\mathbf{L}$ obtained from the proposed FDD.

3.3. Fault Detection and Diagnosis

The proposed FDD algorithm includes two stages. In the first stage, adaptive Extended Kalman Filters (aEKFs) are used to estimate the motor rotation speed and the drag coefficient, based on speed measurements. We used the proposed aEKF algorithm in [42] and developed the first stage based on the motor dynamics by defining $\mathbf{x}_m = \begin{bmatrix}\omega & d\end{bmatrix}^\top$:

$$\dot{\mathbf{x}}_m = \begin{bmatrix} -k_1 x_1 - k_2 x_2 x_1^2 + k_3 I_m \\ 0 \end{bmatrix} = \mathbf{f}_m(\mathbf{x}, I_m) \tag{47}$$

Thus, the Jacobian is obtained as follows:

$$\mathbf{F}_m = \begin{bmatrix} -k_1 - 2k_2 x_2 x_1 & -k_2 x_1^2 \\ 0 & 0 \end{bmatrix} \tag{48}$$

Moreover, the measurement model is

$$\mathbf{z} = \mathbf{h}(\mathbf{x}_m) + \mathbf{v} = \mathbf{H}\mathbf{x}_m + \mathbf{v} \tag{49}$$

where $\mathbf{H} = \begin{bmatrix}1 & 0\end{bmatrix}^\top$. The equations for the aEKF are adopted from [42]:

$$\mathbf{d}(k) = \mathbf{z}(k) - \mathbf{h}(\hat{\mathbf{x}}_m^-(k)) \tag{50a}$$

$$\mathbf{K}(k) = \mathbf{P}^-(k)\mathbf{H}_k^\top \left[\mathbf{H}(k)\mathbf{P}^-(k)\mathbf{H}^\top(k) + \mathbf{R}(k-1)\right]^{-1} \tag{50b}$$

$$\boldsymbol{\epsilon}(k) = \mathbf{z}(k) - \mathbf{h}(\hat{\mathbf{x}}_m^+(k)) \tag{50c}$$

$$\mathbf{R}(k) = \lambda_m \mathbf{R}(k-1) + (1-\lambda_m)(\boldsymbol{\epsilon}(k)\boldsymbol{\epsilon}^\top(k) + \mathbf{H}(k)\mathbf{P}^-(k)\mathbf{H}^\top(k)) \tag{50d}$$

$$\mathbf{Q}(k) = \lambda_m \mathbf{Q}(k-1) + (1-\lambda_m)(\mathbf{K}(k)\mathbf{d}(k)\mathbf{d}^\top(k)\mathbf{K}^\top(k)) \tag{50e}$$

$$\hat{\mathbf{x}}_m^+(k) = \hat{\mathbf{x}}_m^-(k) + \mathbf{K}(k)\mathbf{d}(k) \tag{50f}$$

$$\mathbf{P}^+(k) = (\mathbf{I} - \mathbf{K}(k)\mathbf{H}(k))\mathbf{P}^-(k)(\mathbf{I} - \mathbf{K}(k)\mathbf{H}(k))^\top + \mathbf{K}(k)\mathbf{R}(k)\mathbf{K}(k)^\top \tag{50g}$$

Since the drag coefficient varies due to aerodynamic disturbances, estimating this coefficient is important; otherwise, the LoE fault estimation becomes inaccurate. Considering that most actuators have a similar gain of ω^2, denoted as $k_2\alpha$, we calculate the median of all estimated k_2 values to find an equivalent drag coefficient, $\bar{d}$. In the second stage, we develop an OS-ELM algorithm to estimate the LoE fault gains.

To design the OS-ELM for the second stage, the nominal model of the inner loop dynamics and motor dynamics are used. Hence, the corresponding model can be represented as follows:

$$\bar{\mathbf{y}} = \mathbf{M}^\top \boldsymbol{\alpha} \tag{51}$$

where

$$\bar{\mathbf{y}} = \begin{bmatrix} \ddot{\mathbf{x}} - \mathbf{F}(\dot{\mathbf{x}}) \\ \dot{\omega} + k_1\omega - k_3 \mathbf{I}_m \end{bmatrix} \tag{52a}$$

$$\mathbf{M} = \begin{bmatrix} \mathbf{B}(\mathbf{x})\mathbf{G}\ \mathrm{diag}(\mathbf{u}_c) \\ -k_2\ \mathrm{diag}\left(\begin{bmatrix}\omega_1^2, \ldots, \omega_{N_R}^2\end{bmatrix}\right) \end{bmatrix} \tag{52b}$$

Furthermore, the following recursive equations are used in the GOS-ELM method [26]:

$$\hat{\boldsymbol{\alpha}}(k) = \hat{\boldsymbol{\alpha}}(k-1) + \mathbf{N}(k)\mathbf{M}(k)\left(\bar{\mathbf{y}}(k) - \mathbf{M}^\top(k)\hat{\boldsymbol{\alpha}}(k-1)\right) \tag{53}$$

$$\begin{aligned} \mathbf{N}(k) = & \frac{\mathbf{N}(k-1)}{\lambda} \\ & - \frac{\mathbf{N}(k-1)}{\lambda}\mathbf{M}(k)\left(\lambda\mathbf{I} + \mathbf{M}^\top(k)\mathbf{N}(k-1)\mathbf{M}(k)\right)^{-1}\mathbf{M}^\top(k)\mathbf{N}(k-1) \end{aligned} \tag{54}$$

where $\hat{\boldsymbol{\alpha}}$ represents the estimated fault coefficients and $0 < \lambda \leq 1$ is a forgetting factor. Therefore, the actuator health vector $\boldsymbol{\alpha}$ can be estimated using the Algorithm 1. Additionally, the overall structure of the proposed FDD is depicted in Figure 5.

3.4. Safety Filter

To ensure flight safety, the safety constraints must first be determined and then enforced. To this end, a safety filter is developed utilizing control barrier functions to meet this requirement.

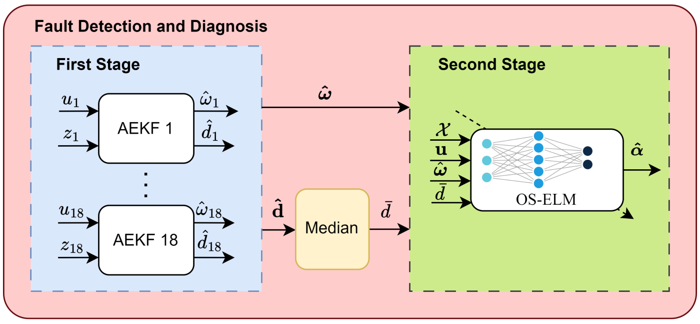

Figure 5: Overall view of the proposed FDD block

Algorithm 1 Proposed FDD algorithm

Initialization:
Set the initial state estimate $\hat{\mathbf{x}}_m^+(0)$ and covariance $\mathbf{P}^+(0)$. ▷ see Eqs. (50f, 50g)
Set the initial noise covariances $\mathbf{Q}(0)$ and $\mathbf{R}(0)$.
Set the initial $\mathbf{N}(0)$. ▷ see Eq. (54)
Choose forgetting factors λ and λ_m.
for each time step k **do**
  for each motor j **do**
    Prediction Step:
    $\hat{\mathbf{x}}_m^-(k) = \hat{\mathbf{x}}_m^+(k-1) + T_s \mathbf{f}_m(\hat{\mathbf{x}}_m^+(k-1), I_m(k-1))$.
    $\mathbf{P}^-(k) = \mathbf{F}_{d,m}(k-1)\mathbf{P}^+(k-1)\mathbf{F}_{d,m}^\top(k-1) + \mathbf{Q}(k-1)$.
    Correction Step:
    Compute the Kalman gain $\mathbf{K}(k)$. ▷ see Eq. (50b)
    Compute the innovation $\mathbf{d}(k)$. ▷ see Eq. (50a)
    Update the state estimate $\hat{\mathbf{x}}_m^+(k)$. ▷ see Eq. (50f)
    Update the covariance $\mathbf{P}^+(k)$. ▷ see Eq. (50g)
    Compute the residual $\boldsymbol{\epsilon}(k)$. ▷ see Eq. (50c)
    Update $\mathbf{R}(k)$. ▷ see Eq. (50d)
    Update $\mathbf{Q}(k)$. ▷ see Eq. 50e)
  end for
  Compute $\bar{d}$.
  Compute $\bar{\mathbf{y}}(k), \mathbf{M}(k)$. ▷ see Eqs. (52a, 52b)
  Update $\mathbf{N}(k)$. ▷ see Eq. (54)
  Update $\hat{\alpha}(k)$. ▷ see Eq. (53)
end for

Consider the following control-affine system:

$$\dot{\mathbf{x}} = \mathbf{f}(\mathbf{x}) + \mathbf{g}(\mathbf{x})\mathbf{u}, \tag{55}$$

where $\mathbf{x} \in \mathbb{R}^n$, $\mathbf{u} \in \mathbb{R}^m$.

Definition 3.1 (CBF [43, 44])**.** A function $h : \mathbb{R}^n \to \mathbb{R}$ is a *Control Barrier Function (CBF)* for the system (55) and the safe set $C = \{\mathbf{x} \in \mathbb{R}^n | h(\mathbf{x}) \geq 0\}$ if there exists $\alpha \in \mathcal{K}_\infty$ such that:

$$\sup_{\mathbf{u} \in \mathbb{R}^m} [\mathcal{L}_f h(\mathbf{x}) + \mathcal{L}_g h(\mathbf{x})\mathbf{u} + \alpha(h(\mathbf{x}))] \geq 0 \quad \forall\ \mathbf{x} \in C. \tag{56}$$

For systems with relative degree $r \geq 1$, higher-order control barrier functions (HOCBFs) are introduced.

Definition 3.2 (HOCBF [43, 44])**.** Define $\psi_0(\mathbf{x}) := h(\mathbf{x})$ and recursively:

$$\psi_i(\mathbf{x}) := \dot{\psi}_{i-1}(\mathbf{x}) + \alpha_i(\psi_{i-1}(\mathbf{x})), \quad i = 1, \ldots, r \tag{57}$$

where $\alpha_i(\cdot)$ are class $\mathcal{K}$ functions. The corresponding sets are:

$$C_i := \{\mathbf{x} \in \mathbb{R}^n : \psi_{i-1}(\mathbf{x}) \geq 0\}, \quad i = 1, \ldots, r \tag{58}$$

A function $h(\mathbf{x})$ is a *High-Order Control Barrier Function* of relative degree r if there exist differentiable class $\mathcal{K}$ functions $\alpha_1, \ldots, \alpha_m$ such that:

$$\psi_r(\mathbf{x}, \mathbf{u}) = \mathcal{L}_f^r h(\mathbf{x}) + \mathcal{L}_g \mathcal{L}_f^{r-1} h(\mathbf{x})\mathbf{u} + O(h(\mathbf{x})) + \alpha_r(\psi_{r-1}(\mathbf{x})) \geq 0 \tag{59}$$

where $O(b(\mathbf{x}))$ contains all lower-order Lie derivatives.

Safety constraints on state variables, such as altitude limits and vertical speed bounds, are enforced through Control Barrier Functions (CBFs), ensuring the air taxi remains within predefined safe regions. Additionally, a CBF is designed to guarantee trajectory containment within a specified corridor around the reference path, even under disturbances and actuator faults. Thus, we consider the following CBFs for ensuring safety:

$$h_1(\mathbf{p}) = d_m^2 - \|\mathbf{e}_\perp\|^2 \geq 0, \tag{60a}$$
$$h_2(z) = z - z_{\min} \geq 0, \tag{60b}$$
$$h_3(v_d) = v_d - v_{d,\min} \geq 0, \tag{60c}$$
$$h_4(v_d) = v_{d,\max} - v_d \geq 0, \tag{60d}$$

where $h_1(\mathbf{p})$, $h_2(z)$, $h_3(v_d)$ and $h_4(v_d)$ are accounting for limiting the maximum cross-track error, maximum altitude, minimum vertical velocity, and maximum vertical velocity, respectively. Moreover, the cross-track error is defined as follows:

$$\mathbf{e}_\perp = \mathbf{P}_\perp(t)\,(\mathbf{p} - \mathbf{p}_d)\,, \tag{61a}$$
$$\mathbf{P}_\perp = \mathbf{I} - \mathbf{T}\mathbf{T}^\top, \tag{61b}$$
$$\mathbf{T} = \frac{\dot{\mathbf{p}}_d}{\|\dot{\mathbf{p}}_d\|}. \tag{61c}$$

The aforementioned cross-track error CBF is to ensure the vehicle's flight path remains within the specified distance from the reference path.

Since an algorithm for estimating the uncertain terms of the system dynamics has already been developed, the obtained information can be utilized to improve the accuracy of the models employed in the safety filter, which functions as adaptive CBFs. Therefore, the translational tracking error dynamics is given by:

$$\ddot{\mathbf{e}}_p = \mathbf{F}_t + \mathbf{G}_t\mathbf{u} + \hat{\mathbf{U}}_t - \ddot{\mathbf{p}}_d, \tag{62a}$$
$$\mathbf{F}_t = \begin{bmatrix} 0 & 0 & g \end{bmatrix}^\top, \tag{62b}$$
$$\mathbf{G}_t = -\frac{1}{m}\begin{bmatrix} \cos\psi\sin\theta\cos\phi + \sin\psi\sin\phi & 0 & 0 & 0 \\ \sin\psi\sin\theta\cos\phi - \cos\psi\sin\phi & 0 & 0 & 0 \\ \cos\phi\cos\theta & 0 & 0 & 0 \end{bmatrix}\mathbf{G}\hat{\mathbf{L}}, \tag{62c}$$

where $\hat{\mathbf{U}}_t = \begin{bmatrix} \hat{U}_x & \hat{U}_y & \hat{U}_z \end{bmatrix}^\top$. Also, $\hat{U}_x$ and $\hat{U}_y$ are obtained from ESO related to horizontal translational dynamics, and $\hat{U}_z$ is obtained from the neural network and disturbance observer. In addition, the estimated fault coefficients $\hat{\mathbf{L}}$ are incorporated into the control design, and the resulting adaptive expressions yield an adaptive control barrier function with improved accuracy in satisfying the constraints under uncertainties.

It should be noted that, given that there are discrepancies in the estimation of the uncertainties and actuator faults, an upper bound must be established for these discrepancies in order to provide a robustness margin for compliance with the constraints by the control barrier functions.

Assumption 3.2. The uncertainty estimation errors $\tilde{U}_i = U_i - \hat{U}_i$ where $i = x, y, z$ are bounded. assuming $\tilde{\mathbf{U}}_t = \begin{bmatrix} \tilde{U}_x & \tilde{U}_y & \tilde{U}_z \end{bmatrix}^\top$, the norm of the uncertainty estimation error is bounded by $||\tilde{\mathbf{U}}_t|| \leq \delta_1$ and $||\tilde{U}_z|| \leq \delta_2$.

Since h_1 and h_2 are HOCBFs, and h_3, h_4 are standard CBFs, the CBF and HOCBF conditions can be written as follows:

$$L_f^2 h_1 + L_g L_f h_1\ \mathbf{u} + k_{2_p}\dot{h}_1 + k_{1_p} h_1 \geq \epsilon_1(\delta_1). \tag{63a}$$
$$L_f^2 h_2 + L_g L_f h_2\ \mathbf{u} + k_{2_z}\dot{h}_2 + k_{1_z} h_2 \geq \epsilon_2(\delta_2). \tag{63b}$$
$$L_f h_3 + L_g h_3 \mathbf{u} + k_3 h_3 \geq \epsilon_3(\delta_2), \tag{63c}$$
$$L_f h_4 + L_g h_4 \mathbf{u} + k_4 h_4 \geq \epsilon_4(\delta_2). \tag{63d}$$

Here, $k_{1_p}, k_{2_p}, k_{1_z}, k_{2_z}, k_3, k_4 > 0$ are scalar gains selected from a linear class-$\mathcal{K}$ function. In addition, $\epsilon_j(\delta_k) > 0$ is a robustness margin accounting for uncertainty estimation error.

Finally, the set of constraints (63a), (63b), (63c) and (63d) can be expressed as follows:

$$\mathbf{A}_{SF}\mathbf{u} \leq \mathbf{b}_{SF}. \tag{64}$$

The safe control input is computed by solving the following Quadratic Programming (QP) problem:

$$\begin{aligned} \underset{\mathbf{u}}{\text{minimize}} \quad & ||\mathbf{u} - \mathbf{u}_{\text{nom}}||^2 \\ \text{subject to} \quad & (64), \\ & \mathbf{u}_{\min} \leq \mathbf{u} \leq \mathbf{u}_{\max}. \end{aligned} \tag{65}$$

Here, $\mathbf{u}_{\text{nom}}$ is a nominal control input from the dynamic control allocation and $\mathbf{u}_{\min}, \mathbf{u}_{\max}$ are actuator bounds. It is worth noting that the QP problem (65) remains feasible when the constraints are appropriately defined; however, it may become infeasible under certain environmental conditions or maneuvers, indicating that no control input exists that can satisfy all constraints simultaneously. This issue is beyond the scope of this research and in such circumstances, only the same input $\mathbf{u}_{\text{nom}}$ is applied to the actuators.

3.5. Outer-Loop Control

The outer loop is responsible for controlling the horizontal position and tracking the path. In this paper, it is assumed that the reference path is known and the goal is to track it with appropriate accuracy.

The horizontal position dynamics can be written as follows:

$$\ddot{\mathbf{p}}_h = \begin{bmatrix} \ddot{x} \\ \ddot{y} \end{bmatrix} = \begin{bmatrix} u_x \\ u_y \end{bmatrix} + \begin{bmatrix} d_x \\ d_y \end{bmatrix}, \tag{66}$$

where d_x and d_y denote the disturbances in the horizontal position dynamics. By defining $\mathbf{h}_1 = [\, x \quad y \,]^\top$, $\mathbf{h}_2 = [\, \dot{x} \quad \dot{y} \,]^\top$, and $\mathbf{u}_{xy} = \begin{bmatrix} u_x & u_y \end{bmatrix}^\top$,

the ESO is designed to estimate the disturbance in the horizontal position dynamic as follows:

$$\dot{\hat{\mathbf{h}}}_1 = \hat{\mathbf{h}}_2 + \lambda_2(\mathbf{h}_1 - \hat{\mathbf{h}}_1) \tag{67a}$$
$$\dot{\hat{\mathbf{h}}}_2 = \mathbf{u}_{xy} + \hat{\mathbf{h}}_3 + \lambda_1(\mathbf{h}_1 - \hat{\mathbf{h}}_1) \tag{67b}$$
$$\dot{\hat{\mathbf{h}}}_3 = \lambda_0(\mathbf{h}_1 - \hat{\mathbf{h}}_1), \tag{67c}$$

where $\boldsymbol{\lambda}_i \in \mathbb{R}^2$ and $\mathbf{h}_3$ represent the observer gain matrix and disturbance vector, respectively.

Therefore, by designing the matrix gains, the error dynamics can be matched with Hurwitz polynomials and therefore achieving bounded estimation error [45].

Thus, by defining the tracking error of horizontal position as $\mathbf{e}_h = \mathbf{h}_1 - \mathbf{p}_{h_d}$, the outer-loop control law is a PD controller augmented with ESO for robust performance:

$$\mathbf{u}_{xy} = \begin{bmatrix} \ddot{x}_d \\ \ddot{y}_d \end{bmatrix} - \begin{bmatrix} K_{P_x} & 0 \\ 0 & K_{P_y} \end{bmatrix} \mathbf{e}_h - \begin{bmatrix} K_{D_x} & 0 \\ 0 & K_{D_y} \end{bmatrix} \dot{\mathbf{e}}_h - \hat{\mathbf{h}}_3 \tag{68}$$

where the gains $K_{P_x}, K_{D_x}, K_{P_y}$ and K_{D_y} are positive. The desired roll and pitch angles can be obtained from the acceleration control input $\mathbf{u}_{xy}$ as follows:

$$\phi_{d,c} = \sin^{-1}\left(-\frac{m}{F_T}(u_x \sin\psi - u_y \cos\psi)\right) \tag{69a}$$
$$\theta_{d,c} = \sin^{-1}\left(-\frac{m\left(u_x \cos\psi + u_y \sin\psi\right)}{F_T \cos\phi_{d,c}}\right) \tag{69b}$$

Finally, after calculating the desired roll and pitch angle commands from (69), a saturation block is applied to these angles so that the final desired angles are within a certain range for safe and optimal vehicle performance.

4. Results

A detailed nonlinear simulation of the multirotor eVTOL air taxis is employed in this research to evaluate the performance of the designed control system. The simulations are performed in MATLAB/Simulink. Regarding the NN, a RBF neural network with a single hidden layer is employed. The hidden layer consists of 30 neurons, each initialized with randomly assigned centers in the range $[-1 \ \ 1]$ and widths in the range $[1.1 \ \ 2.2]$. The initial weights of the network are set to zero.

Since the nominal model (24) used by the controller includes only the total mass and moments of inertia, up to 20% random uncertainty is considered in these parameters. Moreover, aerodynamic effects, gyroscopic effects, and other phenomena that are not in the nominal model are considered as unmodeled dynamics. To evaluate the robustness of the proposed control system, severe wind gusts and turbulence are applied to the air taxi.

Specifically, a steady wind of magnitude $V_{w,s} = 1$ m/s with a direction of 70° and a reference wind shear of magnitude $V_{sh,ref} = 10$ m/s with a direction of 70° were applied, while turbulence with a magnitude of $W_{20} = 10$ m/s and a direction of 10° was generated using the Dryden model. Furthermore, gusts in all three directions with magnitudes of $u_{g,m} = 5, v_{g,m} = 4, w_{g,m} = 2$ m/s and durations of 10, 20, and 30 seconds, respectively, starting at times 50, 100, and 162 seconds, were applied (see Appendix A). The time history of the applied overall wind velocity can be seen in Figure 6.

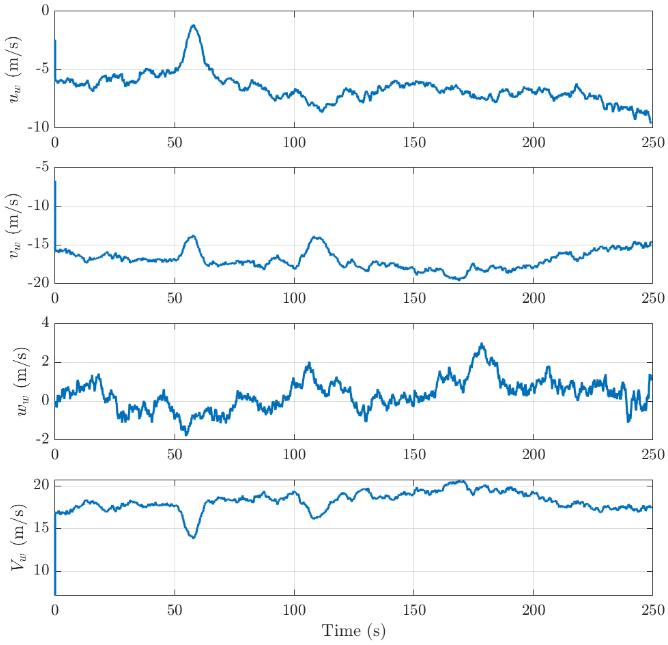

Figure 6: Applied wind velocity components in the local coordinate system and its magnitude

In addition, an external disturbance signal was added to the torques acting on the vehicle as (70):

$$[\mathbf{m}_d]^B = \begin{bmatrix} 0.1\sin\left(\frac{\pi}{5}t + \frac{\pi}{7}\right) \\ 0.1\sin\left(\frac{\pi}{7}t\right) \\ 0.02\cos\left(\frac{\pi}{8}t + \frac{\pi}{3}\right) \end{bmatrix} \tag{70}$$

Moreover, the actuator faults are applied as follows:

$$\begin{aligned} &\alpha_1 = 0 && \text{for } t \geq 40\,\text{s} \\ &\alpha_3 = 0,\ \alpha_6 = 1 - 0.01(t-90) && \text{for } t \geq 90\,\text{s} \\ &\alpha_{14} = 0,\ \alpha_{18} = 0,\ \alpha_6 = 0.5 && \text{for } t \geq 140\,\text{s} \\ &\alpha_7 = 0,\ \alpha_{11} = 0,\ \alpha_{16} = 0.6 && \text{for } t \geq 180\,\text{s}. \end{aligned} \tag{71}$$

The fault coefficients (71) act on the forces and drag moment as follows:

$$\bar{f}_j = \alpha_j f_j, \tag{72a}$$
$$\bar{\tau}_j = \alpha_j \tau_j, \tag{72b}$$
$$\bar{H}_j = \alpha_j H_j, \tag{72c}$$

The controller's parameters are chosen as listed in Table 1.

To evaluate and compare the quality of trajectory tracking and uncertainty estimation, the Mean Absolute Error (MAE), Root-Mean-Square Error (RMSE), Relative Root-Mean-Square Error (RRMSE), and Normalized Mean Absolute Uncertainty Estimation Error (NMAUEE) metrics are defined as follows:

$$\mathrm{MAE}(\mathbf{e}) = \frac{1}{T}\int_0^T |\mathbf{e}|\,\mathrm{d}t, \tag{73a}$$
$$\mathrm{RMSE}(\mathbf{e}) = \sqrt{\frac{1}{T}\int_0^T \mathbf{e}^\top\mathbf{e}\,\mathrm{d}t}, \tag{73b}$$
$$\mathrm{RRMSE}(\mathbf{e}, \mathbf{x}_d) = \sqrt{\frac{\int_0^T \mathbf{e}^\top\mathbf{e}\,\mathrm{d}t}{\int_0^T \mathbf{x}_d^\top\mathbf{x}_d\,\mathrm{d}t}} \times 100\%, \tag{73c}$$
$$\mathrm{NMAUEE}(\mathbf{U}, \hat{\mathbf{U}}) = \frac{\int_0^T \|\tilde{\mathbf{U}}\|\,\mathrm{d}t}{\int_0^T \|\mathbf{U}\|\,\mathrm{d}t} \times 100\%, \tag{73d}$$

where T is the simulation time, $\mathbf{U}$ represents the sum of the state-dependent and control-dependent uncertainties, and time-dependent disturbances, $\hat{\mathbf{U}}$ represents its estimate, and $\tilde{\mathbf{U}}$ represents its estimation error:

$$\tilde{\mathbf{U}} = \hat{\mathbf{U}} - \mathbf{U} \tag{74a}$$
$$\mathbf{U} = \mathbf{\Delta}(\mathcal{X}, \boldsymbol{\nu}) + \mathbf{d}(t) = \ddot{\mathbf{x}} - \mathbf{F}(\dot{\mathbf{x}}) - \mathbf{B}(\mathbf{x})\boldsymbol{\nu} \tag{74b}$$
$$\hat{\mathbf{U}} = \hat{\mathbf{W}}^\top\boldsymbol{\mu}(\mathcal{X}, \boldsymbol{\nu}) + \hat{\mathbf{D}}_M \odot \tanh\left(\frac{\mathbf{e}_c}{\epsilon_e}\right) \tag{74c}$$

Additionally, $\mathbf{U}_h$ denotes the total uncertainty in the horizontal dynamic, while $\hat{\mathbf{U}}_h$ and $\tilde{\mathbf{U}}_h$ represent its estimate and estimation error, respectively.

Moreover, control effort is defined as follows:

$$\mathrm{CE} = \sqrt{\frac{1}{T}\int_0^T \mathbf{u}^\top\mathbf{u}\,\mathrm{d}t} \tag{75}$$

In the following, different flight scenarios are considered to assess the effectiveness of the proposed approach.

4.1. Controller Performance

To better evaluate the quality of trajectory and attitude tracking, the criterion values under different conditions are presented in Table 2. These conditions include: (1) only unmodeled dynamics and parametric uncertainties, (2) the addition of disturbances and noise along with uncertainties, and (3) the introduction of faults in addition to all previous factors. It can be observed that criterion values increase as additional sources of uncertainty are introduced. In particular, disturbances lead to a significant rise in position tracking errors, whereas faults primarily increase attitude tracking errors. Moreover, the simulation result of trajectory tracking for the last scenario is shown in Figure 7. It can be seen that the air taxi can satisfactorily follow the desired 3D trajectory despite uncertainties, disturbances, and actuator faults.

Table 1: Numerical values of the control system's parameters

Parameters	Value	Parameters	Value	Parameters	Value	Parameters	Value
Γ	2	k_c	8	λ_m	0.956	k_3	3
N_n	30	k_s	0.6	λ_f	0.985	k_4	3
k_D	0.3	K_{P_x}	0.2	k_{1_p}	2	ζ	0.6
λ	1	K_{P_y}	0.2	k_{2_p}	3	ω_n	8
λ_s	6	K_{D_x}	0.45	k_{2_z}	3		
$\mathbf{K}$	diag ([6 6 4 4])	K_{D_y}	0.45	k_{1_z}	2		

Table 2: Numerical comparison of the control systems performance in different scenarios

Scenario	MAE (x)	MAE (y)	MAE (z)	RRMSE ($\mathbf{\Phi}$)	RRMSE ($\mathbf{p}$)
Uncertainty	0.95 m	0.64 m	0.07 m	0.9%	0.27%
Uncertainty + Disturbance + Noise	1.26 m	1.45 m	0.16 m	1.48%	0.33%
Uncertainty + Disturbance + Noise + Fault	1.28 m	1.46 m	0.15 m	2.37%	0.34%

4.2. *Uncertainty Estimation Performance*

Furthermore, the time history of the uncertainty estimation by the inner-loop and outer-loop controllers in the last scenario is shown in Figure 8, which illustrates a decreasing trend. In addition, the final values of the NMAUEE metric for the entire scenario are NMAUEE($\mathbf{U}$) = 10.85% and NMAUEE($\mathbf{U}_h$) = 12.19%.

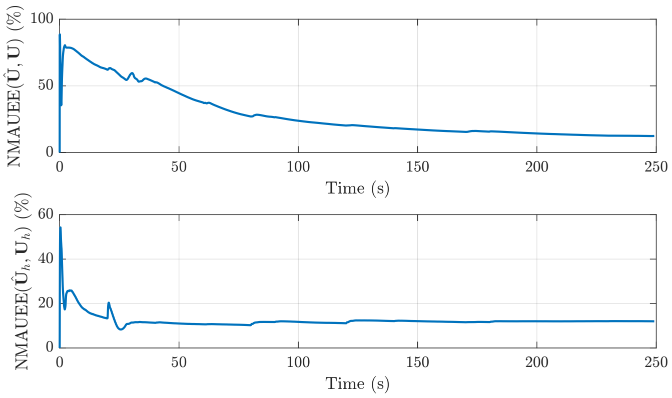

Figure 8: Time history of NMAUEE in both inner and outer control loops

To evaluate the effect of the augmented ESO on the outer-loop PD controllers, the simulation results with and without the ESO are presented in Table 3. As shown, the proposed method achieves a significant improvement in tracking accuracy.

Table 3: Numerical comparison of adding ESO on the controller performance

Approach	MAE (x)	MAE (y)	MAE (z)	RRMSE ($\mathbf{p}$)
PD	1.87 m	2.90 m	0.12 m	0.41%
ESO-PD	1.28 m	1.46 m	0.15 m	0.34%

4.3. *FDD Performance*

As demonstrated in Figure 9, the fault gain estimation performance of the proposed FDD algorithm can be observed. It can be concluded that the proposed FDD algorithm is capable of detecting and estimating simultaneous faults with acceptable accuracy (less than 20% estimation error) despite severe aerodynamic disturbances acting on the propellers' forces and moments. It is worth noting that the oscillations in the estimated gains can be attributed to the degrading estimation performance of the drag moment coefficient (d) by AEKFs.

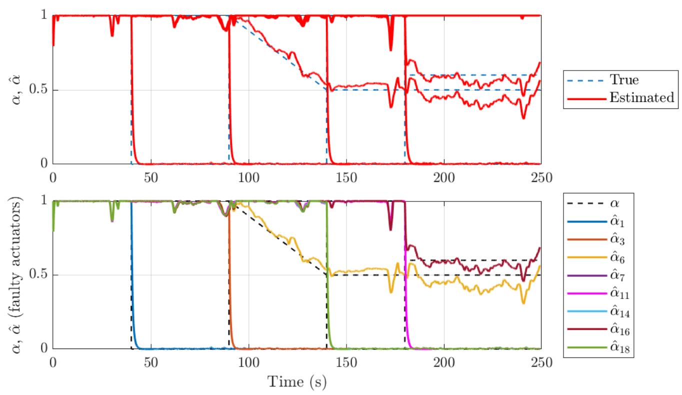

Figure 9: Fault gain estimation performance of the proposed FDD algorithm

4.4. *Dynamic Control Allocation Effect Analysis*

To analyze the effect of the proposed dynamic control allocation with the FDD algorithm, the approach is evaluated in two configurations: with static control allocation (CANCDO-SCA) and with dynamic control allocation (CANCDO-DCA). The results of their performance in attitude tracking are illustrated in Figure 10. Since the control input is used as the input to the neural network, the uncertainties caused by faults can be estimated and compensated for. This allows the method to capture the total uncertainty even without employing dynamic control allocation.

Furthermore, the numerical criteria for a clearer comparison are presented in Table 4. These results show that in trajectory tracking, the static control allocation achieves relatively better performance, whereas in the attitude tracking, the dynamic control allocation provides consistently superior results.

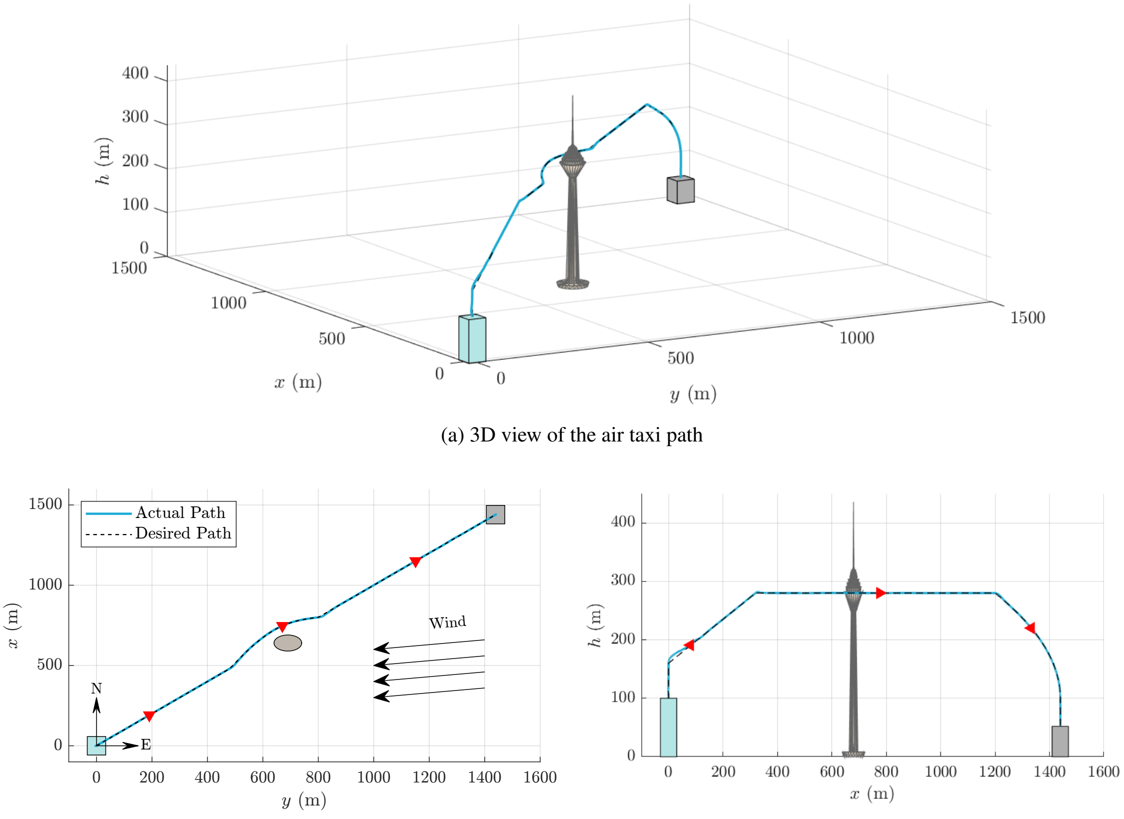

(a) 3D view of the air taxi path

(b) Up view in the horizontal plane

(c) Side view in the vertical plane

Figure 7: The air taxi trajectory in the realistic flight condition

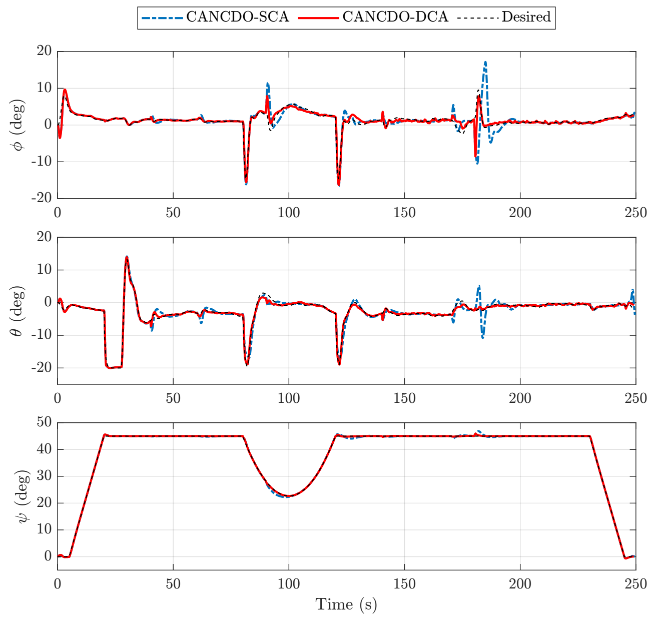

Figure 10: Comparison of attitude tracking performance between CANCDO-SCA and CANCDO-DCA

It should also be noted that when static control allocation is applied, the uncertainties caused by faults are indirectly compensated through additional virtual control commands generated based on the tracking error, as demonstrated in Figure 11. However, this leads to increased control effort, as noted in Table 4.

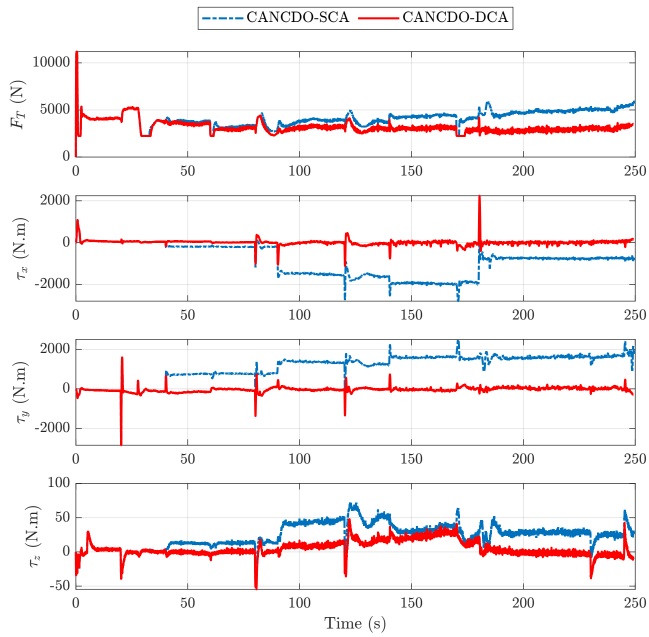

Figure 11: Generated virtual control commands in CANCDO-SCA and CANCDO-DCA

Table 4: Numerical comparison of controller performance between CANCDO-SCA and CANCDO-DCA

Approach	MAE (x)	MAE (y)	MAE (z)	RRMSE ($\mathbf{\Phi}$)	RRMSE ($\mathbf{p}$)	CE
CANCDO-SCA	1.35 m	1.59 m	0.12 m	8.64%	0.35%	1022 N
CANCDO-DCA	1.28 m	1.46 m	0.15 m	2.37%	0.34%	881 N

4.5. Safety Filter Performance

To evaluate the effectiveness of the proposed safety filter, a severe horizontal gust with a magnitude of 34 m/s is applied at 150 seconds for a duration of 10 seconds. In addition, a vertical gust with a magnitude of 9 m/s is introduced at 162 seconds, also lasting for 10 seconds. This scenario is simulated both with and without the safety filter, and the results are shown in Figure 12. It can be concluded that all CBFs in the safety filter are capable of maintaining the safety constraints in the presence of considered environmental disturbances and actuator faults.

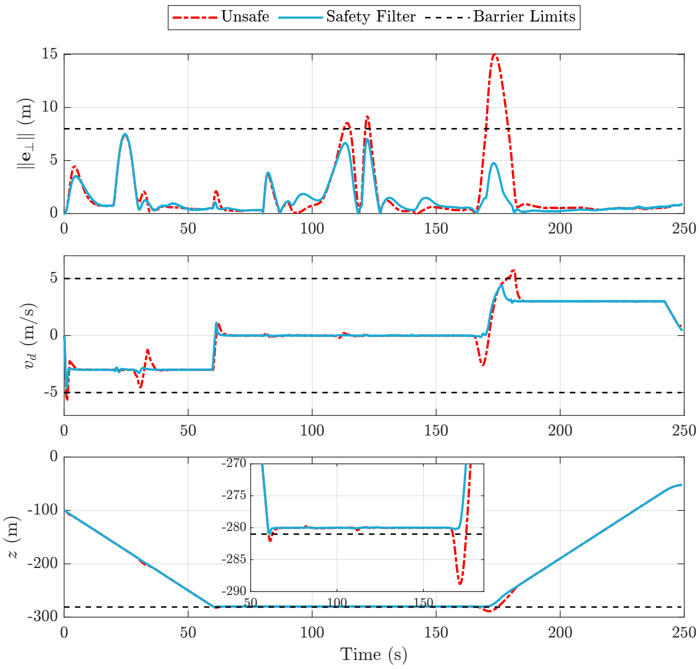

Figure 12: Impact of safety filters under predefined constraints

5. Conclusion

A safe adaptive neural control system was introduced in this paper. The proposed control method employed a Composite Learning-based Adaptive Neural Control with Disturbance Observer (CANCDO) for attitude and altitude control and an ESO-augmented PD controller for position control. Stability of the proposed control system was analyzed based on the Lyapunov's stability theorem. The disturbance observer compensates for external disturbances and neural network estimation errors, while a state observer is used to enhance network learning. The dynamic control allocation block is responsible for optimal distributions of the virtual control commands based on the actuator's health. Finally, the proposed control system was applied to a realistic dynamic model of an multirotor eVTOL air taxi. According to the obtained simulation results, using the developed control sysytem, the air taxi is capable of safe tracking the desired trajectory in a 3D environment under different types of model uncertainties, external disturbances, actuator faults, and measurement noises. Although the proposed control scheme demonstrated satisfactory performance in handling uncertainties during trajectory tracking in the presented simulations, future research should focus on developing supervisory control and trajectory planning frameworks that enable intelligent decision-making under various flight conditions and regulatory constraints. Another promising direction is the design of more robust, physics-informed fault detection and diagnosis algorithms for enhanced system reliability. In addition, advancing data-driven control barrier functions (CBFs) to address collision avoidance, no-fly zones, and other safety-critical constraints represents an important avenue for future work.

Declaration of Competing Interests

The authors declare that they have no known competing financial interests or personal relationships that could have appeared to influence the work reported in this paper.

Declaration of AI Assistance in the Writing Process

During manuscript preparation, the authors used ChatGPT solely to improve language and readability. After using this tool, the authors reviewed and edited the content as needed and take full responsibility for the content of the publication.

Appendix A. Wind Modeling Details

It is assumed that there is a constant horizontal wind with frame A and velocity $\mathbf{v}_A^E$ exists, which generally varies with height. In addition, a gust with frame G and velocity $\mathbf{v}_G^A$, is defined to move relative to the constant wind frame. Finally, the motion of turbulent air particles with frame T and velocity $\mathbf{v}_T^G$ is considered, moving relative to the frame G. As a result, the overall air motion $\mathbf{v}_@^E$ is expressed in the local coordinate system as follows:

$$\left[\mathbf{v}_@^E\right]^L = \left[\mathbf{v}_A^E\right]^L + \left[\mathbf{v}_G^A\right]^L + \left[\mathbf{v}_T^G\right]^L. \tag{A.1}$$

For modeling wind shear, the Surface Wind model [46] is employed. In this model, the Earth's surface is assumed to be fixed relative to the surrounding atmosphere, and a horizontal wind develops within the boundary layer, with its speed increasing as altitude increases [46]:

$$V_{w,sh} = V_{sh,\text{ref}} \frac{\ln\left(h_{\text{AGL}}/h_0\right)}{\ln\left(h_{\text{ref}}/h_0\right)}, \tag{A.2}$$

where h_{AGL}, h_{ref} and $V_{sh,\text{ref}}$ represents the height above the ground in feet, the reference height above the surface, and the reference velocity at this height, respectively. In addition, according to [47], the values of $h_{\text{ref}} = 20$ ft and $h_0 = 0.15$ ft are considered for flight at altitudes between approximately 1 meter and 300 meters. Thus, the horizontal wind has a constant component $V_{w,s}$ and a height-dependent component for wind shear $V_{w,sh}$, expressed in local coordinate system as follows:

$$\left[\mathbf{v}_A^E\right]^L = \left[-(V_{w,s} + V_{w,sh})\cos\psi_w \quad -(V_{w,s} + V_{w,sh})\sin\psi_w \quad 0\right]. \tag{A.3}$$

Furthermore, the $1 - \cos$ gust model [48] in three directions is considered in this work:

$$V_g(t) = \begin{cases} \frac{V_{g,m}}{2}\left(1 - \cos\left(\frac{2\pi}{T_g}(t - t_0)\right)\right) & t_0 < t < t_0 + T_g, \\ 0 & \text{Otherwise} \end{cases}, \tag{A.4}$$

where $V_{g,m}$, T_g, and t_0 represent the gust amplitude, gust duration, and gust duration time, respectively.

To model the turbulence, the Dryden model is used, which can be expressed in terms of shaping filters. According to [47] for heights less than 300 meters, the turbulence intensity is modeled as follows:

$$\sigma_w = 0.1 W_{20} \tag{A.5a}$$

$$\frac{\sigma_u}{\sigma_w} = \frac{\sigma_v}{\sigma_w} = \frac{1}{(0.177 + 0.000823h)^{0.4}}, \tag{A.5b}$$

where where h and W_{20} represent the height in feet and the wind speed at a height of 20 feet, respectively. Therefore, by applying band-limited white noise as input to the filters, the turbulence velocities in three directions can be obtained.

Appendix B. Stability Analysis

To prove the closed-loop system stability of the inner-loop and the candidate Lyapunov function is considered as follows:

$$V = \frac{1}{2}\mathbf{s}_m^\top \mathbf{s}_m + \frac{1}{2}k_s \mathbf{s}_s^\top \mathbf{s}_s + \frac{1}{2\Gamma}\operatorname{Tr}\left(\tilde{\mathbf{W}}^\top \tilde{\mathbf{W}}\right) + \frac{1}{2k_D}\tilde{\mathbf{D}}_M^\top \tilde{\mathbf{D}}_M, \tag{B.1}$$

where $\tilde{\mathbf{W}} = \hat{\mathbf{W}} - \mathbf{W}^*$ and $\tilde{\mathbf{D}}_M = \hat{\mathbf{D}}_M - \mathbf{D}_M^*$. In addition, $\operatorname{Tr}(\cdot)$ represents the trace function of the matrix.

Assuming the optimal neural network weights and the disturbance upper bound are constant, one has $\dot{\tilde{\mathbf{W}}} = \dot{\hat{\mathbf{W}}}$ and $\dot{\tilde{\mathbf{D}}}_M = \dot{\hat{\mathbf{D}}}_M$. Thus, by differentiating the Lyapunov function (B.1), it is obtained that:

$$\begin{aligned} \dot{V} &= \mathbf{s}_m^\top \dot{\mathbf{s}}_m + k_s \mathbf{s}_s^\top \dot{\mathbf{s}}_s + \frac{1}{\Gamma}\operatorname{Tr}\left(\tilde{\mathbf{W}}^\top \dot{\hat{\mathbf{W}}}\right) + \frac{1}{k_D}\tilde{\mathbf{D}}_M^\top \dot{\hat{\mathbf{D}}}_M \\ &= \mathbf{s}_m^\top\left(-\tilde{\mathbf{W}}^\top \boldsymbol{\mu} + \mathbf{D} - \hat{\mathbf{D}}_M \odot \operatorname{sign}(\mathbf{e}_c) - \mathbf{K}\mathbf{s}_m\right) \\ &+ k_s \mathbf{s}_s^\top\left(\tilde{\mathbf{W}}^\top \boldsymbol{\mu} + \hat{\mathbf{D}}_M \odot \operatorname{sign}(\mathbf{e}_c) - \mathbf{D} - k_c \mathbf{s}_s\right) \\ &+ \frac{1}{\Gamma}\operatorname{Tr}\left(\tilde{\mathbf{W}}^\top \dot{\hat{\mathbf{W}}}\right) + \frac{1}{k_D}\tilde{\mathbf{D}}_M^\top \dot{\hat{\mathbf{D}}}_M. \end{aligned} \tag{B.2}$$

By substituting (37a) and (37b) into (B.2), we obtain:

$$\begin{aligned} \dot{V} =& \mathbf{s}_m^\top\left(-\tilde{\mathbf{W}}^\top \boldsymbol{\mu} + \mathbf{D} - \hat{\mathbf{D}}_M \odot \operatorname{sign}(\mathbf{e}_c) - \mathbf{K}\mathbf{s}_m\right) \\ &+ k_s \mathbf{s}_s^\top\left(\tilde{\mathbf{W}}^\top \boldsymbol{\mu} + \hat{\mathbf{D}}_M \odot \operatorname{sign}(\mathbf{e}_c) - \mathbf{D} - k_c \mathbf{s}_s\right) \\ &+ \operatorname{Tr}\left(\tilde{\mathbf{W}}^\top \boldsymbol{\mu}\left(\mathbf{s}_m^\top - k_s \mathbf{s}_s^\top\right)\right) + \tilde{\mathbf{D}}_M^\top |\mathbf{e}_c|. \end{aligned} \tag{B.3}$$

Using the property $\operatorname{Tr}(\mathbf{b}\mathbf{a}^\top) = \mathbf{a}^\top \mathbf{b}$, where $\mathbf{a}_{n\times1} = \mathbf{s}_m$ and $\mathbf{b}_{n\times1} = \tilde{\mathbf{W}}^\top \boldsymbol{\mu}$, it follows that:

$$\begin{aligned} \dot{V} =& \mathbf{s}_m^\top\left(-\tilde{\mathbf{W}}^\top \boldsymbol{\mu} + \mathbf{D} - \hat{\mathbf{D}}_M \odot \operatorname{sign}(\mathbf{e}_c) - \mathbf{K}\mathbf{s}_m\right) \\ &+ k_s \mathbf{s}_s^\top\left(\tilde{\mathbf{W}}^\top \boldsymbol{\mu} + \hat{\mathbf{D}}_M \odot \operatorname{sign}(\mathbf{e}_c) - \mathbf{D} - k_c \mathbf{s}_s\right) \\ &+ \mathbf{s}_m^\top \tilde{\mathbf{W}}^\top \boldsymbol{\mu} - k_s \mathbf{s}_s^\top \tilde{\mathbf{W}}^\top \boldsymbol{\mu} + \tilde{\mathbf{D}}_M^\top |\mathbf{e}_c| \\ =& \mathbf{s}_m^\top\left(\mathbf{D} - \hat{\mathbf{D}}_M \odot \operatorname{sign}(\mathbf{e}_c) - \mathbf{K}\mathbf{s}_m\right) \\ &+ k_s \mathbf{s}_s^\top\left(\hat{\mathbf{D}}_M \odot \operatorname{sign}(\mathbf{e}_c) - \mathbf{D} - k_c \mathbf{s}_s\right) + \tilde{\mathbf{D}}_M^\top |\mathbf{e}_c| \\ =& -\mathbf{s}_m^\top \mathbf{K}\mathbf{s}_m - k_s \mathbf{s}_s^\top k_c \mathbf{s}_s - \mathbf{e}_c^\top\left(\hat{\mathbf{D}}_M \odot \operatorname{sign}(\mathbf{e}_c) - \mathbf{D}\right) + \tilde{\mathbf{D}}_M^\top |\mathbf{e}_c|. \end{aligned} \tag{B.4}$$

Considering $\mathbf{e}_c^\top \mathbf{D} \leq |\mathbf{e}_c^\top| \mathbf{D}_M^*$ and transposing the scalar terms, (B.4) can be rewritten as follows:

$$\begin{aligned} \dot{V} \leq& -\mathbf{s}_m^\top \mathbf{K}\mathbf{s}_m - k_s \mathbf{s}_s^\top k_c \mathbf{s}_s - \mathbf{e}_c^\top \hat{\mathbf{D}}_M \odot \operatorname{sign}(\mathbf{e}_c) + |\mathbf{e}_c^\top| \mathbf{D}_M^* + \tilde{\mathbf{D}}_M^\top |\mathbf{e}_c| \\ =& -\mathbf{s}_m^\top \mathbf{K}\mathbf{s}_m - k_s \mathbf{s}_s^\top k_c \mathbf{s}_s - \left(\hat{\mathbf{D}}_M - \mathbf{D}_M^*\right)^\top |\mathbf{e}_c| + \tilde{\mathbf{D}}_M^\top |\mathbf{e}_c|, \end{aligned} \tag{B.5}$$

Hence, it is obtained:

$$\dot{V} \leq -\mathbf{s}_m^\top \mathbf{K}\mathbf{s}_m - k_s \mathbf{s}_s^\top k_c \mathbf{s}_s, \tag{B.6}$$

which indicates the asymptotic stability of the closed-loop system. As a result, both tracking error and uncertainty estimation error will converge to zero and remain bounded.

References

[1] Vertical Flight Society, eVTOL aircraft directory, https://evtol.news/aircraft, accessed 2024-09-15 (2024).

[2] L. Hu, X. Yan, Y. Yuan, Development and challenges of autonomous electric vertical take-off and landing aircraft, Heliyon 11 (1). doi:10.1016/j.heliyon.2024.e41055.

[3] M. D. Pavel, Understanding the control characteristics of electric vertical take-off and landing (evtol) aircraft for urban air mobility, Aerospace Science and Technology 125 (2022) 107143. doi:10.1016/j.ast.2021.107143.

[4] J. Kim, S. A. Gadsden, S. A. Wilkerson, A comprehensive survey of control strategies for autonomous quadrotors, Canadian Journal of Electrical and Computer Engineering 43 (1) (2019) 3–16. doi:10.1109/CJECE.2019.2920938.

[5] B. Wang, Y. Shen, Y. Zhang, Active fault-tolerant control for a quadrotor helicopter against actuator faults and model uncertainties, Aerospace Science and Technology 99 (2020) 105745. doi:10.1016/j.ast.2020.105745.

[6] T. P. Nascimento, M. Saska, Position and attitude control of multi-rotor aerial vehicles: A survey, Annual Reviews in Control 48 (2019) 129–146. doi:10.1016/j.arcontrol.2019.08.004.

[7] N. P. Nguyen, N. Xuan Mung, S. K. Hong, Actuator fault detection and fault-tolerant control for hexacopter, Sensors 19 (21) (2019) 4721. doi:10.3390/s19214721.

[8] B. Wang, Y. Zhang, An adaptive fault-tolerant sliding mode control allocation scheme for multirotor helicopter subject to simultaneous actuator faults, IEEE Transactions on Industrial Electronics 65 (5) (2017) 4227–4236. doi:10.3390/aerospace9060304.

[9] J. Su, H. Huang, H. Zhang, Y. Wang, F.-Y. Wang, evtol performance analysis: A review from control perspectives, IEEE Transactions on Intelligent Vehiclesdoi:10.1109/TIV.2024.3387405.

[10] C.-H. Pi, K.-C. Hu, S. Cheng, I.-C. Wu, Low-level autonomous control and tracking of quadrotor using reinforcement learning, Control Engineering Practice 95 (2020) 104222. doi:10.1016/j.conengprac.2019.104222.

[11] C. Fu, W. Hong, H. Lu, L. Zhang, X. Guo, Y. Tian, Adaptive robust backstepping attitude control for a multi-rotor unmanned aerial vehicle with time-varying output constraints, Aerospace Science and Technology 78 (2018) 593–603. doi:10.1016/j.ast.2018.05.021.

[12] S. A. Emami, P. Castaldi, A. Banazadeh, Neural network-based flight control systems: Present and future, Annual Reviews in Control 53 (2022) 97–137. doi:10.1016/j.arcontrol.2022.04.006.

[13] B. Xu, Z. Shi, C. Yang, F. Sun, Composite neural dynamic surface control of a class of uncertain nonlinear systems in strict-feedback form, IEEE transactions on cybernetics 44 (12) (2014) 2626–2634. doi:10.1109/TCYB.2014.2311824.

[14] S. A. Emami, A. Banazadeh, P. Hajipourzadeh, P. Castaldi, S. A. Fazelzadeh, Disturbance observer-based adaptive neural guidance and control of an aircraft using composite learning, Control Engineering Practice 134 (2023) 105463. doi:10.1016/j.conengprac.2023.105463.

[15] G. Lai, Z. Liu, Y. Zhang, C. P. Chen, Adaptive position/attitude tracking control of aerial robot with unknown inertial matrix based on a new robust neural identifier, IEEE Transactions on Neural Networks and Learning Systems 27 (1) (2016) 18–31. doi:10.1109/TNNLS.2015.2406812.

[16] L. Brunke, M. Greeff, A. W. Hall, Z. Yuan, S. Zhou, J. Panerati, A. P. Schoellig, Safe learning in robotics: From learning-based control to safe reinforcement learning, Annual Review of Control, Robotics, and Autonomous Systems 5 (1) (2022) 411–444. doi:10.1146/annurev-control-042920-020211.

[17] M. Saied, H. Shraim, C. Francis, A review on recent development of multirotor uav fault-tolerant control systems, IEEE Aerospace and Electronic Systems Magazinedoi:10.1109/MAES.2023.3327697.

[18] N. P. Nguyen, S. K. Hong, Sliding mode thau observer for actuator fault diagnosis of quadcopter uavs, Applied Sciences 8 (10) (2018) 1893. doi:10.3390/app810189.

[19] Z. Cen, H. Noura, T. B. Susilo, Y. A. Younes, Robust fault diagnosis for quadrotor uavs using adaptive thau observer, Journal of Intelligent & Robotic Systems 73 (2014) 573–588. doi:10.1007/s10846-013-9921-8.

[20] F. Xu, J. Tan, X. Wang, V. Puig, B. Liang, B. Yuan, Mixed active/passive robust fault detection and isolation using set-theoretic unknown input observers, IEEE Transactions on Automation Science and Engineering 15 (2) (2017) 863–871. doi:10.1109/TASE.2017.2776998.

[21] W. Jung, H. Bang, Fault and failure tolerant model predictive control of quadrotor uav, International Journal of Aeronautical and Space Sciences 22 (3) (2021) 663–675. doi:10.1007/s42405-020-00331-1.

[22] M. Frangenberg, J. Stephan, W. Fichter, Fast actuator fault detection and reconfiguration for multicopters, in: AIAA guidance, navigation, and control conference, 2015, p. 1766. doi:10.2514/6.2015-1766.

[23] D. Asadi, Model-based fault detection and identification of a quadrotor with rotor fault, International Journal of Aeronautical and Space Sciences 23 (5) (2022) 916–928. doi:10.1007/s42405-022-00494-z.

[24] A. Altinors, F. Yol, O. Yaman, A sound based method for fault detection with statistical feature extraction in uav motors, Applied Acoustics 183 (2021) 108325. doi:10.1016/j.apacoust.2021.108325.

[25] D. A. Andrioaia, V. G. Gaitan, Finding fault types of bldc motors within uavs using machine learning techniques, Heliyon 10 (9). doi:10.1016/j.heliyon.2024.e30251.

[26] S. A. Emami, A. Banazadeh, Fault-tolerant predictive trajectory tracking of an air vehicle based on acceleration control, IET Control Theory & Applications 14 (5) (2020) 750–762. doi:10.1049/iet-cta.2019.0596.

[27] S. Ijaz, C. Fuyang, M. T. Hamayun, Adaptive non-linear integral sliding mode fault-tolerant control allocation scheme for octorotor uav system, IET Control Theory & Applications 14 (19) (2020) 3139–3156. doi:10.1049/iet-cta.2020.0476.

[28] N. P. Nguyen, N. Xuan Mung, L. N. N. T. Ha, S. K. Hong, Fault-tolerant control for hexacopter uav using adaptive algorithm with severe faults, Aerospace 9 (6) (2022) 304. doi:10.3390/en12010095.

[29] S. P. Madruga, T. P. Nascimento, F. Holzapfel, A. M. Lima, Estimating the loss of effectiveness of uav actuators in the presence of aerodynamic effects, IEEE Robotics and Automation Letters 8 (3) (2023) 1335–1342. doi:10.1109/LRA.2023.3238184.

[30] A. Khattab, I. Mizrak, H. Alwi, Fault tolerant control of an octorotor uav using sliding mode for applications in challenging environments, Annual Reviews in Control 57 (2024) 100952. doi:10.1016/j.arcontrol.2024.100952.

[31] M. Khan, M. Zafar, A. Chatterjee, Barrier functions in cascaded controller: Safe quadrotor control, in: 2020 American Control Conference (ACC), IEEE, 2020, pp. 1737–1742. doi:10.23919/ACC45564.2020.9147864.

[32] P. H. Zipfel, Modeling and simulation of aerospace vehicle dynamics, Aiaa, 2014. doi:10.2514/4.102509.

[33] R. Gill, R. D'Andrea, Computationally efficient force and moment models for propellers in uav forward flight applications, Drones 3 (4) (2019) 77. doi:10.3390/drones3040077.

[34] T-MOTOR, U15L Combo Pack Manned Aircraft Type UAV Motor 43KV, https://store.tmotor.com/product/u15l-manned-aircraft-combo.html, accessed 2025-03-10 (2025).

[35] J. S. Hayden, The effect of the ground on helicopter hovering power required, in: Proc. AHS 32nd Annual Forum, 1976, 1976, =https://api.semanticscholar.org/CorpusID:115406795.

[36] X. He, G. Kou, M. Calaf, K. K. Leang, In-ground-effect modeling and nonlinear-disturbance observer for multirotor unmanned aerial vehicle control, Journal of dynamic systems, measurement, and control 141 (7) (2019) 071013. doi:10.1115/1.4043221.

[37] D. Gauthier, N. Biederman, B. Gyovai, J. Wilhelm, Digital twin of a dc brushless electric motor-propeller system with application to drone dynamics, in: AIAA SCITECH 2024 Forum, 2024, p. 2359. doi:10.2514/6.2024-2359.

[38] N.-y. Liang, G.-b. Huang, P. Saratchandran, N. Sundararajan, A fast and accurate online sequential learning algorithm for feedforward networks, IEEE Transactions on Neural Networks 17 (6) (2006) 1411–1423. doi:10.1109/TNN.2006.880583.

[39] M. M. Polycarpou, Stable adaptive neural control scheme for nonlinear systems, IEEE Transactions on Automatic control 41 (3) (1996) 447–451. doi:10.1109/9.486648.

[40] R. Rysdyk, A. J. Calise, Robust nonlinear adaptive flight control for consistent handling qualities, IEEE Transactions on Control Systems Technology 13 (6) (2005) 896–910. doi:10.1109/TCST.2005.854345.

[41] R. Rysdyk, A. Calise, Fault tolerant flight control via adaptive neural network augmentation, in: Guidance, navigation, and control conference and exhibit, 1998, p. 4483. doi:10.2514/6.1998-4483.

[42] S. Akhlaghi, N. Zhou, Z. Huang, Adaptive adjustment of noise covariance in kalman filter for dynamic state estimation, in: 2017 IEEE power & energy society general meeting, IEEE, 2017, pp. 1–5. doi:10.1109/PESGM.2017.8273755.

[43] M. Cohen, C. Belta, Adaptive and learning-based control of safety-critical systems, Springer, 2023. doi:10.1007/978-3-031-29310-8.

[44] A. D. Ames, X. Xu, J. W. Grizzle, P. Tabuada, Control barrier function based quadratic programs for safety critical systems, IEEE Transactions on Automatic Control 62 (8) (2016) 3861–3876. doi:10.1109/TAC.2016.2638961.

[45] M. Ramírez-Neria, A. Luviano-Juárez, J. González-Sierra, R. Ramírez-Juárez, J. Aguerrebere, E. G. Hernandez-Martinez, Active disturbance rejection control for the trajectory tracking of a quadrotor, in: Actuators, Vol. 13, MDPI, 2024, p. 340. doi:10.3390/act13090340.

[46] R. Bencatel, A. Girard, M. Abdelhafiz, J. Sousa, Shear wind estimation, in: AIAA Guidance, navigation, and control conference, 2011, p. 6224. doi:10.2514/6.2011-6224.

[47] D. McLean, Automatic flight control systems, Measurement and control 36 (6) (2003) 172–175. doi:10.1177/002029400303600602.

[48] B. Wang, M. Warner, A. Tian, L. Scotzniovsky, J. T. Hwang, A comparative study of uncertainty quantification methods in gust response analysis of a lift-plus-cruise evtol aircraft wing, in: AIAA SCITECH 2025 Forum, 2025, p. 2819. doi:10.2514/6.2025-2819.